INVESTIGATING DISLOCATION STRUCTURE EVOLUTION DURING NANOINDENTATION

BY

HASSAAN ZAFAR

A Thesis Presented to the
DEANSHIP OF GRADUATE STUDIES

KING FAHD UNIVERSITY OF PETROLEUM & MINERALS

DHAHRAN, SAUDI ARABIA

In Partial Fulfillment of the
Requirements for the Degree of

MASTER OF SCIENCE

In

MECHANICAL ENGINEERING

MAY 2014

KING FAHD UNIVERSITY OF PETROLEUM & MINERALS

DHAHRAN- 31261, SAUDI ARABIA

DEANSHIP OF GRADUATE STUDIES

This thesis, written by **HASSAAN ZAFAR** under the direction his thesis advisor and approved by his thesis committee, has been presented and accepted by the Dean of Graduate Studies, in partial fulfillment of the requirements for the degree of **MASTER OF SCIENCE IN MECHANICAL ENGINEERING.**

Dr. Shafique Khan
(Advisor)

Dr. Zuhair Gasem
Department Chairman

Dr. Numan Abu-Dheir
(Member)

Dr. Salam A. Zummo
Dean of Graduate Studies

Dr. Sulaman Pashah
(Member)

13/5/14
Date

Dedicated to

My Parents and my wife

ACKNOWLEDGMENTS

First of all I would like to thank Almighty Allah (S.W.T) for giving the strength necessary to achieve my goals. Secondly, I express gratitude to my thesis advisor, Dr. Shafique Khan for his guidance and support throughout the thesis work. He has been very kind, encouraging and a source of inspiration to me. Moreover, I would also like to thank my committee members Dr. Numan Abu-Dheir and Dr. Sulaman Pashah for their valuable suggestions and guidance. I would also like express my gratitude to KFUPM and the Mechanical Engineering Department for their support.

I am also grateful to my university fellows for helpful discussions and advices. Finally, I express thanks to my family for the encouragement and prayers.

TABLE OF CONTENTS

LIST OF TABLES

LIST OF FIGURES

ABSTRACT

Full Name : Hassaan Zafar

Thesis Title : Investigating Dislocation Structure Evolution during Nanoindentation

Major Field : Mechanical Engineering

Date of Degree : May 2014

Dislocation structure evolution during nanoindentation is investigated using a three-dimensional multi-scale discrete dislocation plasticity model. This model combines two length scales, discrete dislocation dynamics and continuum finite element analysis. The multiplication, growth and movement of dislocations on different slip planes, in the vicinity of the nanoindentation site, are studied. Moreover, topographical maps of the nanoindented surface are generated to observe the patterns formed by exiting dislocations. Nanoindentation models are developed for spherical, cylindrical, conical and Berkovich indenter tips. Different initial configurations of dislocation sources are employed in the study.

It is observed that the dislocation activity significantly depends upon the initial configuration of the dislocation sources. Secondly, the orientation of the crystal influences the topography of the nanoindented surface. The accuracy of nanoindentation size effect model developed based on two-dimensional simulations is also investigated. It is found that the hardness results for two-dimensional simulations deviate from those of the three-dimensional model. This is because the important phenomena of cross-slip and strain hardening are ignored in two-dimensional models.

.

ملخص الرسالة

الاسم الكامل: حسان ظفر

عنوان الرسالة: البحث في ظهور و تطور الخلل خلال الغرز بالنانو

التخصص: الهندسة الميكانيكية

تاريخ الدرجة العلمية: مايو 2014

لقد تم دراسة تنامي الخلل الحاصل في المواد خلال عملية الغرز بالنانو بإستخدام نظرية مرونة الخلل ثلاثية الأبعاد. هذه النظرية تعتمد على بعدي طول و ديناميكية الخلل وتحليل العناصر المحدودة. تم دراسة تضاعف و نمو و حركة الخلل في محيط منطقة الغرز. و من ثم تم رسم طوبوغرافيا للسطح المغروس لملاحظة الترتيب الذي أحدثه الخلل. تم إستحداث نظرية غرس لكل من رأس الغرس الكروي و الأسطواني و المخروطي و البيركوفيج . تم توظيف المصادر المتعددة للخلل في الدراسة.

لقد لوحظ أن نشاظ الخلل يعتمد بشكل كبير على طبيعة المصدر الأساسي (المنشأ) لهذا الخلل. و لقد لوحظ أيضاً أن إتجاه البلورات في المادة تؤثر على طبوغرافية السطح المغروز بالنانو. إنّ دقة نظرية تأثير حجم الغرز بالنانو طُورت بالإعتماد على المحاكاة ثنائية الأبعاد. لقد وجد أن قيم الصلادة قد إنحرفت عن المفروض لو تم اعتماد النظرية ثلاثية الأبعاد و ذلك لأنه تم تجاهل أهمية مفهوم الإنزلاق المتقاطع و التقوية بالسلاسة في نظرية الأبعاد الثنائية.

CHAPTER 1

INTRODUCTION

Nanoindentation has become a very popular technique to determine the mechanical properties of materials (e.g. hardness and elastic modulus). However, nanoindentation tests cannot directly explain the mechanisms that occur within the material and their effect on the test results. Investigation of the region around the indentation can help us understand how the plasticity initiates and progresses. According to dislocation theory, plastic deformation is directly related to the nucleation, multiplication and movement of dislocations. However, spatial resolution available through advanced electron microscopy is not enough to experimentally study this nucleation and multiplication of dislocations within the nanoindentation zone, during the nanoindentation test. Therefore, the dislocation activity related to a particular slip system cannot be studied experimentally. This has led to the use of modeling and simulation techniques by researchers to explain the dislocation behavior during nanoindentation Modeling and simulation techniques have been used by researchers to explain the dislocation behavior during nanoindentation. These techniques include: (i) Atomistic/Molecular Dynamics (MD) modeling (ii) Discrete Dislocation Dynamics (*DD*) modeling (iii) Finite Element Methods. Atomistic/MD modeling requires extreme computational power and therefore can only simulate the initial stages of the plastic deformation, i.e. the onset of plasticity, at which neither the dislocation structures have fully developed, nor has the dislocation density

increased considerably. Moreover, only the nanometer scale is considered since the specimen is defined by only a few thousand atoms. Due to these factors, this method cannot simulate the interaction of a large number of dislocations, associated with the plastic deformations during nanoindentation. On the other hand, *DD* modeling can simulate a large number of dislocations.

Two-dimensional discrete dislocation dynamics models have been used by several researchers but these models have limitations as they are simplified with assumptions and cannot simulate detailed analysis of dislocation activity on all slip systems especially the intersecting slip planes. Moreover, the 2D models consider only edge dislocations disregarding screw or mixed character dislocations.

1.1 Nanoindentation Testing

Nanoindentation test apparatus is widely available now. The typical parts include a loading frame, indenter shaft, loading actuator and sensors to measure positions and displacements. An optical microscope is also installed to accurately position the indenter. Nanoindentation testing can be performed on very small volumes of materials and single crystals. The specimen surface must be well prepared to minimize surface roughness for better results. The commonly used indenter tips have spherical, conical, cylindrical or pyramidal shapes. The most common indenter material is diamond that has been ground into the desired tip geometry. Moreover, the onset of plasticity and subsequent plastic deformations are also topics of interests among researchers. Nanoindentation advances the macro and micro indentation tests by indenting on the nanometer length scale. The

resolutions for measuring the displacements and positions are very high. Real time load-displacement data is recorded and plotted while the indentation test is in progress (Fig. 1.1). These curves can be used to extract mechanical properties of the material, such as the hardness and modulus of elasticity. It is very crucial to measure the contact area accurately for best results. This is achieved by imaging the residual impression with a surface probe such as Atomic Force Microsocopy (AFM). The contact area can also be estimated by calculations, if the tip geometry and the final indentation depth is known. In this case, the depth of penetration is recorded, and the area of the indent is determined using the known geometry of the indentation tip.

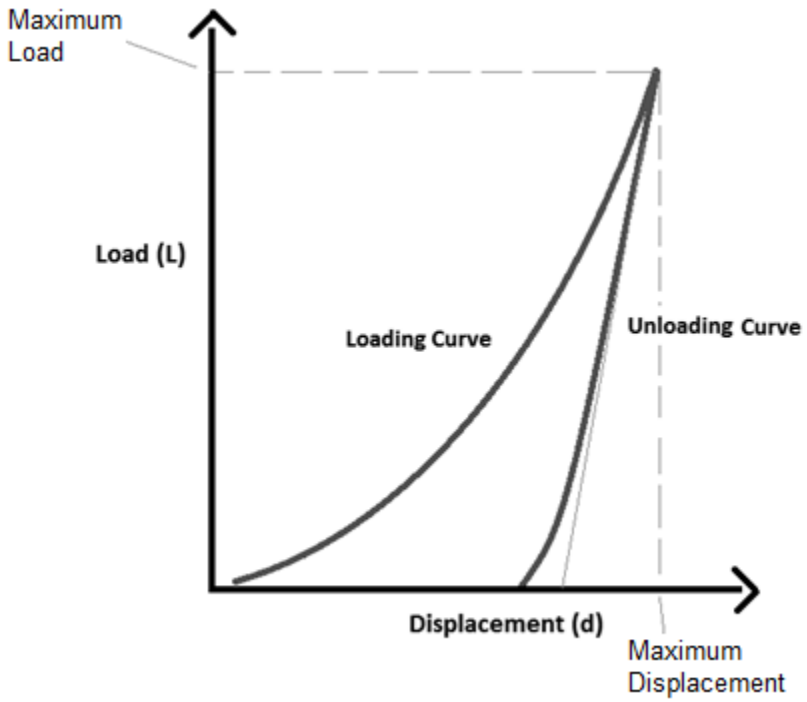

Figure 1.1: Typical load-displacement curve for an instrumented nanoindentation test.

1.2 Dislocation Theory

A dislocation is a crystallographic line defect, or irregularity, within a crystal structure. Dislocations can be envisioned as being caused by the termination of a plane of atoms in the middle of a crystal. In such a case, the neighboring planes are not straight, but instead bent around the edge of the terminating plane. Therefore, the crystal structure is perfectly ordered on both sides of the plane. The dislocation has two properties, a line sense, that defines the direction of the dislocation line, and the Burgers vector that describes the magnitude and direction of distortion to the lattice. Two main types of dislocations exist: (i) edge dislocation (the Burgers vector is perpendicular to the line sense; Fig. 1.2a) (ii) screw dislocation (the Burgers vector is parallel to the line sense; Fig. 1.2b). Dislocations found in real materials are typically mixed, meaning that they have characteristics of both. The Burgers vector in this case lies at an angle to the line sense and thus has both the screw and edge components. When external stress is applied, the dislocations move on their slip planes (by gliding motion) in specific directions, causing plastic deformation. Both Face-Centered Cubic (FCC) and Body-Centered Cubic (BCC) materials have their own specific slip planes and slip directions, combinations of which are called the slip systems. The dislocations interact among themselves to form jogs, junctions, dipoles etc. Moreover, two dislocations with equal Burgers vectors and opposite line senses on the same slip plane can come closer and cancel each other, leaving behind a perfect crystal lattice. This process is called dislocation annihilation. The screw dislocations can slip on to another intersecting slip plane by a process known as cross-slip. Dislocations that account for the plastic deformation during nanoindentation are known as Geometrically Necessary Dislocations (GND).

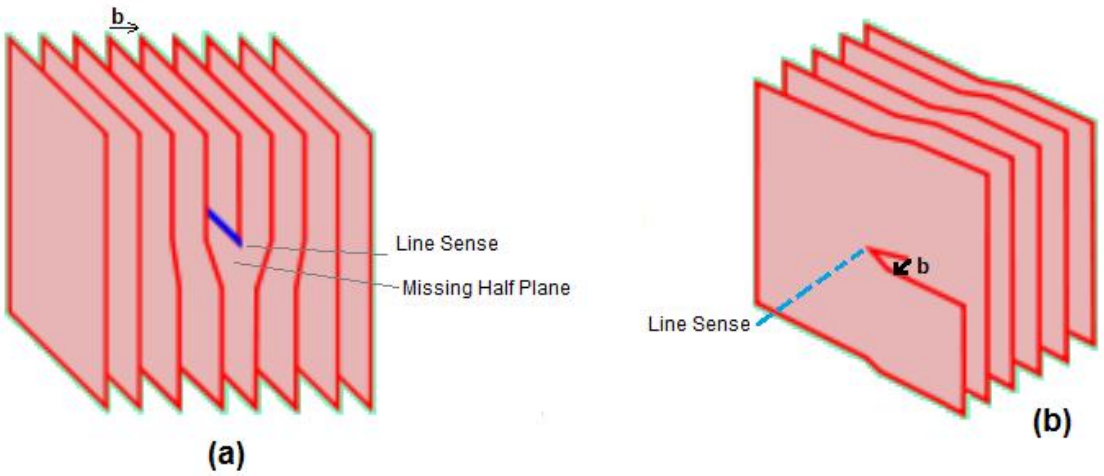

Figure 1.2: (a) Schemetic of an edge dislocation; (b) Schemetic of a screw Dislocation.

1.3 Dislocation Modeling

1.3.1 Discrete Dislocation Dynamics

Discrete Dislocation Dynamics (*DD*) models approximate the dislocation structures by a finite number of discrete dislocations, each with a defined character. *DD* models simulate movement, interaction and multiplication of dislocations when a load is applied. The behavior of an individual dislocation is closely related to the interaction with other dislocations and stresses due to external loadings. In two-dimensional *DD* models, the dislocation structure is approximated by dislocation points with either edge or screw character and usually only one type of slip planes is considered. Therefore for 2D models, the important phenomenon of cross-slip is ignored.

Three dimensional DD models approximate individual dislocation curves by straight line segments. All the slip planes and slip directions can be considered and cross-slip is taken

into account. The motion and interactions of the dislocations is considered in detail on each slip plane.

1.4 Multi-scale Discrete Dislocation Dynamics Plasticity

The three-dimensional Multi-scale Discrete Dislocation Plasticity (*MDDP*) model combines three dimensional *DD* with continuum Finite Element Analyses (*FEA*). The material is considered linear elastic for *FEA*. However, the stresses due to dislocations and plastic strains are superimposed as external loading. The *DD* part simulates the dislocation movement and evolution whereas the *FEA* applies boundary conditions and tracks shape changes of the crystal.

1.5 Research Objectives

The aim of this research is to:

i. Develop models for simulating nanoindentation in the M*DD*P computational code for spherical, flat punch, conical and Berkovich indenters.
ii. Investigate the dislocation structure evolution during nanoindentation using random initial dislocation configuration.
iii. Investigate the dislocation structure evolution during nanoindentation using initial dislocation configuration from atomistic/MD simulation as available in open literature.

iv. Investigate the accuracy of nanoindentation size effect model developed based on 2D simulations.

v. Generate topographical map of nanoindented surface based on exiting dislocations.

1.6 Methodology Followed

Several models were developed for simulating nanoindentation in the *MDDP* computational code for spherical, flat punch, conical and Berkovich indenters using suitable contact mechanics relationships.

Dislocation sources were placed in the computational cell, at different locations, based on different configurations. Indentation loading was applied and a plotting software (Tecplot) was used to visualize the positions of dislocations after each loading step. A computer program was generated and utilized to produce topographical maps based on the density of exiting dislocations at different locations on the nanoindented surface.

CHAPTER 2

LITERATURE REVIEW

2.1 Determination of Mechanical Properties by Nanoindentation

Material response of nanoindentation and related mechanisms is very complicated, especially if heterogeneous and polycrystalline materials are considered. Oliver & Pharr [1, 2] introduced a method for measuring hardness and elastic modulus by instrumented nanoindentation techniques. This technique has been widely adopted and used to determine mechanical behavior on nanoscale because the significance of this technique lies in the fact that the mechanical properties could be determined directly from load-displacement measurements, without the need to image the final impression. For this reason, the method found applications in thin films and small structural elements. Figure 2.1 shows a cross-section through a typical impression made during the nanoindentation test. The material pile up around the indentation site can also be seen.

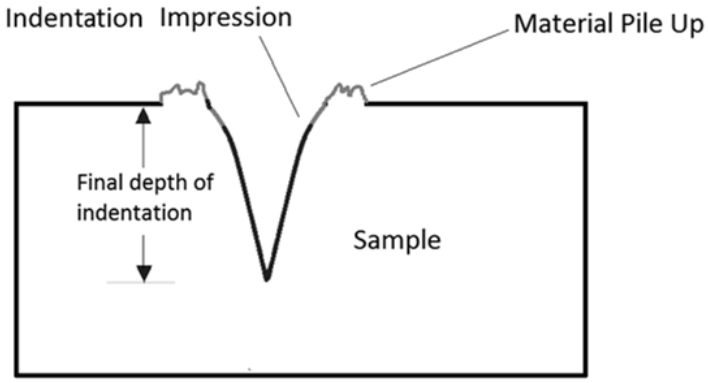

Figure 2.1: Schematic showing section through a typical nanoindentation impression at the end of nanoindentation test.

2.2 Indentation Size Effect

A decrease in hardness with an increase in indentation depth (for sharp tipped indenters) and decrease in hardness with increase in indenter radius (spherical indenters) is known as indentation size effect. Ouyang et al. [3] found that there are at least two effects that account for the size dependence of indentation hardness for circular indentation: strain hardening and the indentation size effect. Kreuzer & Pippan [4] verified through 2D simulation that indentation size effect at small indentation depths is an important effect of the discrete nature of plasticity.

2.3 Pop-In Events/ Excursions

Another interesting phenomenon is the pop-in events, also known as excursions in the load–displacement graphs i.e. there is sudden increase in displacement at constant load during the loading cycle (as shown in Fig. 2.2). Many researchers have investigated this through experiments and simulations. Gane and Bowden [5] were the first to observe the excursion phenomenon on electropolished surfaces of gold, copper and aluminum. Corcoran et al. [6] showed that yielding behavior during nanoindentation on single-crystal gold is composed of a series of discrete yielding events separated by elastic deformation. The pop-ins observed in the load–displacement curves is associated with dislocation emission, particularly homogeneous dislocation nucleation. Barnoush [7] showed that increasing the dislocation density and tip radius, i.e. the region with maximum shear stress below the tip, results in a reduction in the pop-in probability.

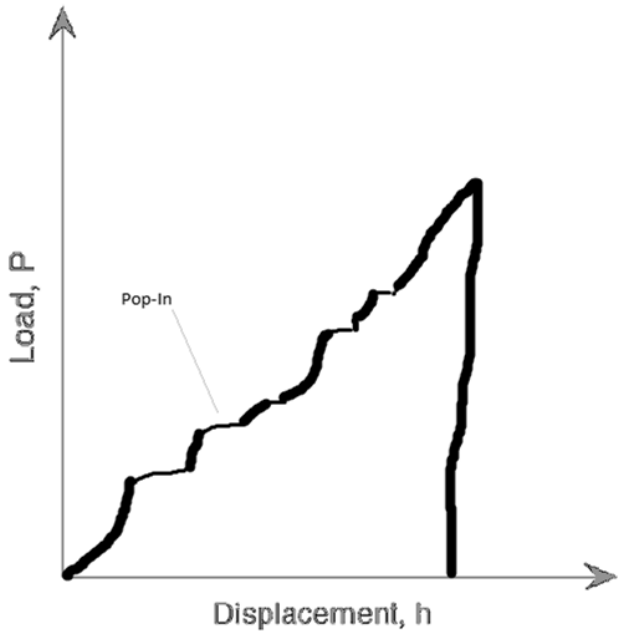

Figure 2.2: Representation of a yielding behavior during nanoindentation with discrete, pop-in events.

2.4 Atomistic/Molecular Dynamics (MD) Simulations

Nanoindentation process has been simulated using atomistic/molecular dynamics modeling. The main focus has been the homogeneous nucleation of dislocations in perfect crystals (without initial defects). Figure 2.3 shows an example of arrangement of atoms in atomistic modeling of nanoindentation. Fuente et al. [8] performed atomistic simulations of the emission of separate dislocation loops by nanoindentation on a (001) FCC surface. They showed that the initial stages of plastic deformation around nanoindentation results in the emission from near the contact point of dislocation half-loops intersecting the surface. Liang et al. [9] investigated elastic–plastic response of a Cu substrate during nanoindentation using molecular dynamics simulation. Wagner et al

[10] modeled nano indentation atomistically and found that smooth indenters nucleate dislocations below the surface but rough indenters can nucleate dislocations both at the surface and below and that increasing temperature from 0K to 300 K creates pre-nucleation defects in the region of high stress and decreases the critical depth. Atomistic simulations cannot simulate a large dislocation structure, since extreme computational power is required.

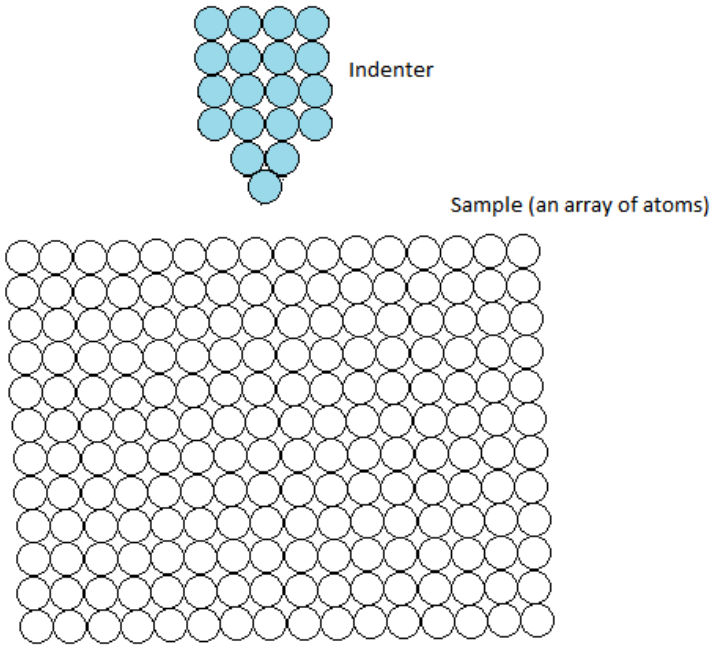

Figure 2.3: Example of arrangement of atoms in atomistic modeling of nanoindentation.

2.5 Nano indentation in Thin Films

Thin films are increasingly used in micro-electromechanical systems and devices. When measuring the nanoindentation hardness of thin films with the thickness of only few microns or nanometers, strong constraint to the dislocation glide in thin film from

substrate must be considered [11-14]. The indentation of thin films usually displays very different behavior from bulk metals. Therefore, it is difficult to measure the mechanical properties of film materials [15]. Influences from the substrate can be ignored when the indentation depth is less than one tenth of the thin film thickness However, it is usually difficult to ensure that the indentation depth is always less than one tenth of the film thickness especially when the thickness of the thin film is on the sub-micron or nanometer order [15-17]. Ouyang et al. [18] used 2D Discrete Dislocation Dynamics to evaluate nanoindentation size effect in thin films, using a simple model.

CHAPTER 3

MODELLING NANOINDENTATION

3.1 Multi-scale Discrete Dislocation Plasticity Model

Multi-scale Discrete Dislocation Plasticity (*MDDP*) is developed by Zbib and co-workers [19-22]. The 3D *DD* model has mesometer length scale and it determines plastic deformation. It evaluates the dislocation motion and interactions, and calculates the associated stresses and strains. The *FEA* model is macro scale and takes care of boundary conditions and shape changes.

In *DD* analysis, the dislocations are approximated by straight line dislocation segments. The Peach Kohler force on a dislocation segment is due to stresses from all other dislocation segments as well as the applied stress. The Peach Kohler force $\mathbf{F}_{j,j+1}$ on a dislocation segment of length *L*, bounded by nodes j and j+1 is given by:

$$\mathbf{F}_{j,j+1} = \left(\sum_{i=1}^{N-1} \frac{1}{L} \int_L \left(\sigma^{D}_{i,i+1} + \sigma^{a}\right).\mathbf{b}_{j,j+1}\right) \times \xi_{j,j+1} dl + \mathbf{F}_{j,j+1\,self} \qquad (1)$$

Where *N* is the total number of dislocation nodes, $\sigma^{D}_{i,i+1}$ is the stress from a distant segment that is bounded by nodes i and i+1. $\xi_{j,j+1}$ is the line sense vector, σ^{a} is the applied stress, $\mathbf{b}_{j,j+1}$ is the Burgers vector and $\mathbf{F}_{j,j+1\,self}$ is the Peach Kohler force due to the local interaction with the neighboring segments.

The net force on a dislocation node is due to contribution from all dislocation segments that are connected to it. All the dislocation nodes move simultaneously in the glide direction over a time increment that is equal to the minimum time required for interaction between two segments. The equation of motion of a dislocation node i is as follows:

$$m_i^* \dot{v}_i + \frac{1}{M_i} \dot{v}_i = \mathbf{F}_{igc} \tag{2}$$

Where m_i^* is the mass per unit dislocation, M_i is the dislocation mobility factor, v_i and $\dot{v}_i$ are the velocity and acceleration of the node i. $\mathbf{F}_{igc}$ is the component of the Peach Kohler force in the direction of dislocation glide.

The motion of each dislocation segment contributes to the overall macroscopic plastic strain $\dot{\boldsymbol{\varepsilon}}^{\mathbf{p}}$ with is calculated by the relation:

$$\dot{\varepsilon}^p = \sum_{i=1}^{N} \frac{l_i v_{gi}}{2V} (\boldsymbol{n_i} \otimes \boldsymbol{b_i} + \boldsymbol{b_i} \otimes \boldsymbol{n_i}) \tag{3}$$

Where *N* is the total number of dislocation nodes l_i is the length of dislocation segment i, $\boldsymbol{n_i}$ is a unit vector normal to slip plane, v_{gi} is the magnitude of glide velocity, $\mathbf{b_i}$ is the Burgers vector and V is the volume of the Representative Volume Element (RVE).

In *DD* analysis, the computational cell is taken to be the RVE with an infinite domain. Either reflection boundary conditions are employed (to keep the dislocation curves continuous) or periodic boundary conditions are employed (to conserve dislocation flux across the boundaries). The *DD* model alone is not suitable for finite domain problems since appropriate boundary conditions cannot be applied using this model. This problem is overcome by the *MDDP* model. In this model, the representative volume element is divided into cubic cells for *DD* analysis. A Finite Element (*FE*) mesh superimposes eight

node brick elements on to the cubic cells. The local stress field due to the dislocations is calculated by *DD* analysis and normalized over each element. The image stresses due to the interaction of dislocations with the finite boundaries are distributed over the surface of the RVE. The plastic strains are also homogenized over the elements. The standard equation in the *FEA* framework is as follows:

$$[\mathbf{M}]\{\ddot{\mathbf{U}}\} + [\mathbf{C}]\{\dot{\mathbf{U}}\} + [\mathbf{K}]\{\mathbf{U}\} = \{\boldsymbol{f}^{\boldsymbol{a}}\} + \{\boldsymbol{f}^{\boldsymbol{B}}\} + \{\boldsymbol{f}^{\infty}\} + \{\boldsymbol{f}^{\boldsymbol{P}}\} \quad (4)$$

Where $\{\mathbf{U}\}$ is the nodal displacement vector and$[\mathbf{M}]$, $[\mathbf{C}]$ and $[\mathbf{K}]$ are the mass, damping and stiffness matrices respectively. $\{\mathbf{f}^{\mathbf{a}}\}$ is the force vector representing external loading, $\{\mathbf{f}^{\mathbf{B}}\}$ is the body force vector from to dislocations interaction, $\{\mathbf{f}^{\infty}\}$ is the force vector from dislocation image stresses and $\{\mathbf{f}^{\mathbf{P}}\}$, is the force vector from plastic strain caused by dislocation motion.

3.2 *MDDP* Simulation Code

MDDP model is developed as a computational mechanics code. It is written in Fortran® programming language. The material properties, initial dislocation configuration, crystal orientation, boundary conditions and external loading scheme are read from the input files. The input files are: Data, *DD*input and *FEA*Conditions. Several modules are available to generate *DD* input files that define distribution of dislocations for both BCC and FCC materials (on all slip systems).

The output files are: Sgtecplot.out, and *FEA*result.out. All files with the extensions '.f' are program files and those with '.h' are header files.

In addition, a file named Restart.file stores the output results after every *DD* time step. This file can be used to resume the *MDDP* program execution in case of unexpected interruption or error during the program execution. The program sequence is shown in Fig. 3.1.

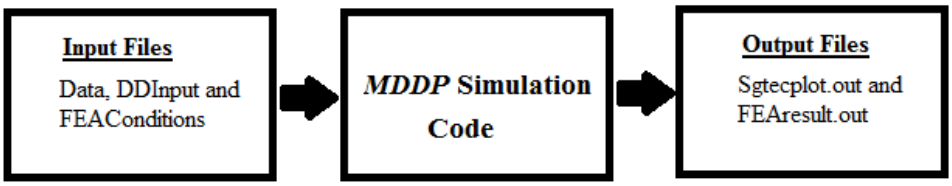

Figure 3.1: The program sequence.

3.2.1 Data and *DD* Input

The file Data contains the following information: (i) The crystal type (FCC or BCC) and the physical properties of the material e.g. the density, shear modulus, Poissons ratio, dislocation mobility, and the magnitude of Burgers vector **b.** (ii) The number of steps (iterations) the program will undergo. (iii) Initial segment length in terms of the magnitude of Burgers vector. (iv) Thermodynamic properties; e.g. temperature, stacking fault energy, thermal conductivity, specific heat capacity etc.(v) Boundary conditions and the conditions for the calculation of stress exerted by dislocations on each other. (vi) Whether *FEA* is to be employed or an infinite domain is to be considered and whether static or dynamic conditions are to be used. (vii) Information regarding point defects. (viii) Defining the coordinate system with respect to the crystal axis. For instance by rotating the axis in such a way that the [111] slip plane of the crystal becomes parallel to

(or coincide with) the x-y plane of the program. If we choose *x*-axis as [100], *y*-axis as [010] and *z*-axis as [001]; this means that the crystal axis coincide exactly with the axis of the program. (viii) The choice of output format (Tecplot or GNU format), and the frequency of updating the output files during the program run. (ix) Whether the iteration time steps are to be constant or variable and whether constant or auto re-meshing is to be used.

3.2.2 Data Output

The output data can be visualized graphically. This is very helpful in order to analyze the displacement of all the dislocation segments with respect to time, in response to the applied stresses and boundary conditions. The graphical output data can be obtained in the GNUplot or TecPlot formats. The file sgtecplot.out records the position and connectivity of dislocation nodes after every time step for use with Tecplot software. It helps to visualize the dislocation vectors in 3D space and creates animated movies of the results. *DD*timeresults.out contains time dependent results like dislocation density, stress, strain etc. *FEA*result.out contains the *FEA* data such as the coordinates of the *FE* nodes, connectivity, nodal displacements and the stress/strain value for each node.

3.3 Nanoindentation in *MDDP*

In the *MDDP* program, the indenter cannot be modeled as a separate physical entity platform because only a single body (the simulation cell) can be considered.

Therefore, nanoindentation can only be modeled by taking into account the loading effect of the indenter on the indented surface. The indenter load is applied on the top surface of

the computational cell on the *FE*s that represents the area of contact between the indenter and the computational cell. The critical thing is to estimate the area of contact corresponding to the varying indentation load for different indenter tip geometries.

Another limitation of *MDDP* program is that the contact area can only be approximated by square-shaped elements on the top surface (see Fig. 3.2) as only cubic shaped brick elements are used in the *FE*. These elements are the top face of the top most *FE*s. The approach followed is that the indentation begins with the center-most element (i.e. element **a**). It progresses on to the nine 3X3 elements (i.e. element **a** and the surrounding eight **b** elements). Further, the contact area is estimated by the twenty five 5X5 (i.e. the elements **a**, **b** and **c**). This procedure can be extended up to 9x9 elements. In this way, the contact area is always square, with its center coinciding with indentation axis.

As opposed to the actual nanoindentation experiments, the value of contact area increases discretely. At the beginning, it is equal to A (i.e. the area of **a**). When indentation continues on to the 3x3 elements, it becomes 9A. Further it becomes 25A for 5x5 elements. Smaller finite elements estimate the contact area better but increase computational effort. Another important factor to be considered is the size and boundary conditions of the RVE. A small computational cell size reduces computational effort. However, it should be large enough such that the sides are not affected by the nanoindentation and it is a truly RVE. The bottom face is considered to have rigid boundary condition and the top surface and the sides have free boundary conditions. The current modeling considers rigid indenters.

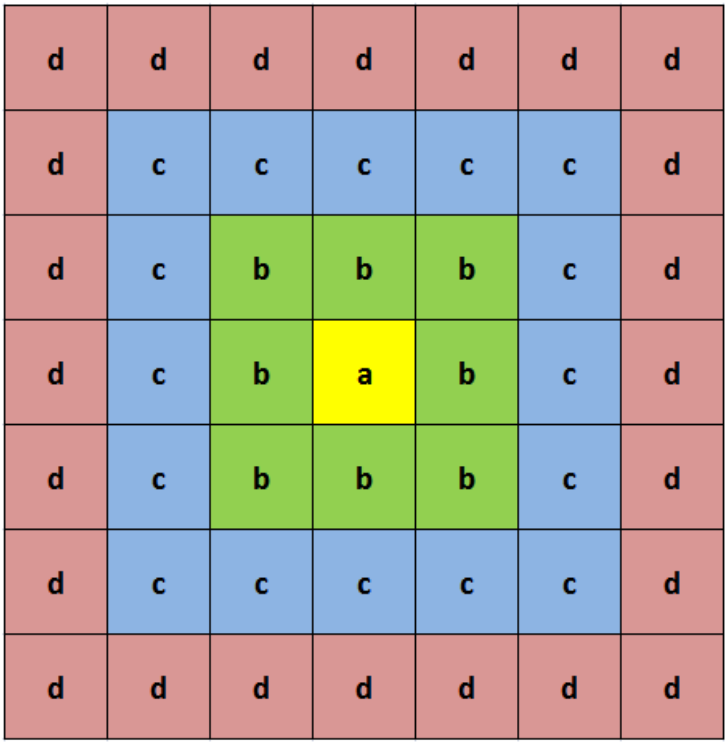

Figure 3.2: The square elements on the top that represent the area of contact.

3.3.1 Nanoindentation Modeling in *MDDP*

Hertz [23] investigated the contact between a spherical indenter and flat surface of a specimen (Fig. 3.3) and devised relationships for indentation depth, contact area and pressure distributions during indentation.

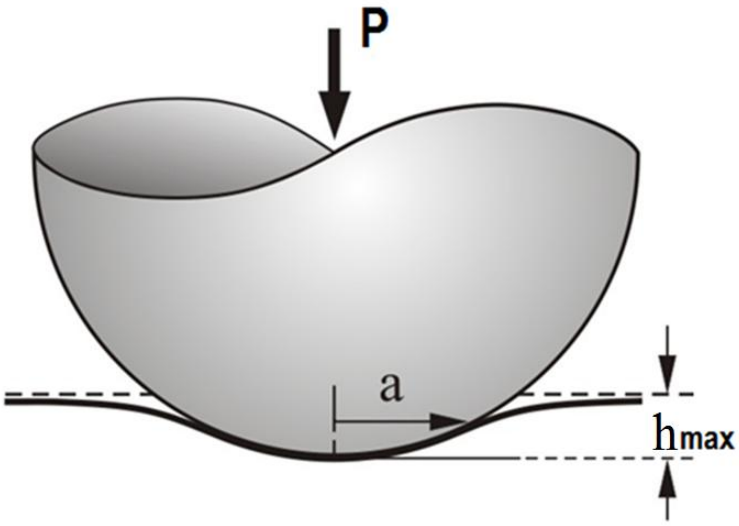

Figure 3.3: Schematic of contact between a sphere and a flat surface.

First, the radius of contact circle a is related to the indenter load P and radius R by the following relation:

$$a^3 = \frac{3}{4}\frac{PR}{E^*} \tag{5}$$

Now, if we consider E and ν to be the elastic modulus and Poissons ratio of the specimen respectively and E′ and ν′ to be the elastic modulus and Poissons ratio of the indenter respectively. The combined modulus E* becomes:

$$\frac{1}{E^*} = \frac{(1-\nu^2)}{E} + \frac{(1-\nu'^2)}{E'} \tag{6}$$

If the indenter is considered to be rigid, the value of E*can be taken as E.

The deflection, h of the surface beneath the indenter is given by:

$$h = \frac{3P}{8E^*a}\left(2 - \left(\frac{r}{a}\right)^2\right) \quad r \leq a \tag{7}$$

Where r is the distance from the center of the contact circle. Eq. 7 shows that the maximum deflection (h_{max}) occurs at r = 0, and the minimum deflection h_{min} occurs at r = a therefore:

$$h_{max} = \frac{3P}{4E^{*}a} \tag{8}$$

$$h_{min} = \frac{3P}{8E^{*}a} \tag{9}$$

Using Eqs. 1 & 4, we can deduce the relation between the indenter load and the maximum depth of penetration:

$$P = \frac{4}{3}E^{*}R^{\frac{1}{2}}h_{max}^{3/2} \tag{10}$$

The pressure distribution for spherical indenter is:

$$p_{sph} = \frac{3P}{2\pi a^{2}}\left(1 - \left(\frac{r}{a}\right)^{2}\right)^{1/2} \tag{11}$$

The maximum pressure below indenter tip (at r = 0) is:

$$p_{sph,max} = \frac{3P}{2\pi a^{2}} \tag{12}$$

3.3.2 Spherical indenter

To calculate the indention parameters, the following steps were followed:

1. The value a in Eq. 5 is calculated by considering a circle of contact radius a and equating it to a square contact area on the top face of RVE,
2. Using the value of a, the indenter load P, is calculated by Eq.5.
3. Using a and P the pressure distribution p_{sph} on circular contact area is calculated by Eq. 11.

4. From the pressure distribution p_{sph} a uniform equivalent pressure $p_{s,eq3D}$ on the area of contact is calculated. This is done by equating the pressure distribution (which has the form of a half ellipsoid) to that of the volume of a cuboid with base area equal to the area of contact of indenter and height equal to $p_{s,eq3D}$ (Fig. 3.4) where:

$$p_{s,eq3D} = \frac{4}{3}\frac{\pi a^2 p_{sph,max}}{2xy} \tag{13}$$

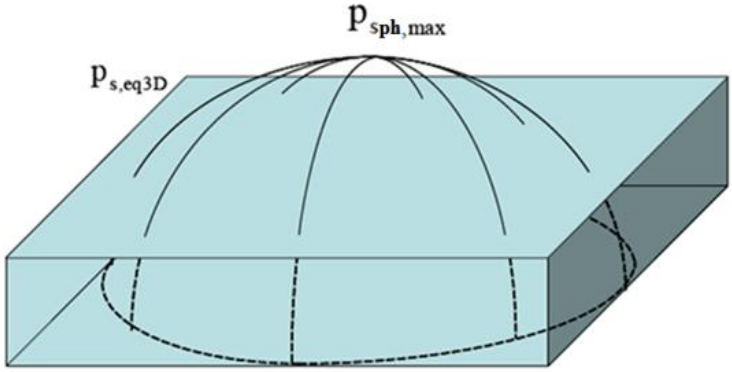

Figure 3.4: Estimation of uniform pressure distribution.

5. The pressure is then applied in ten equal increments during ten consecutive creep time steps.
6. Steps 1-5 are repeated once the indentation progresses from 1x1 elements to 3x3 elements and the pressure increments are added to $p_{s,eq3D}$ for 1x1 indentation. This procedure is repeated again for 5x5 elements and so on. Fig. 3.5 shows the pressure distribution at the end of 5x5 indentation. The center element has the maximum pressure (i.e. $p_{s,max}$).

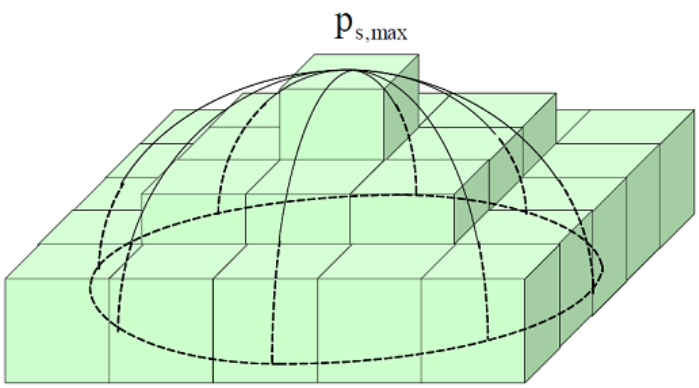

Figure 3.5: The pressure distribution at the end of 5x5 indentation.

The surface displacement profile, just beneath the indenter is plotted and compared with the Hertzian solution (Fig. 3.6). Hertzian curves are plotted only to the extent of the contact area as Hertz theory is only applicable to contact area. It is found that the surface displacement by the spherical indenter model agrees well with the theoretical displacement.

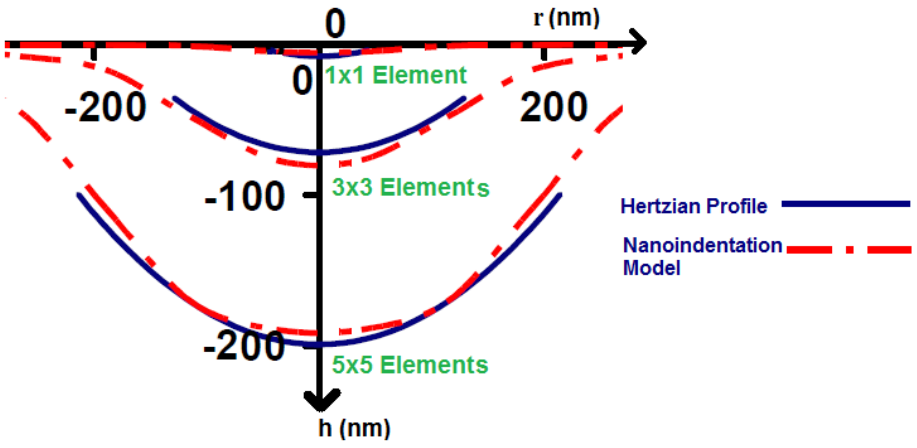

Figure 3.6: Validation of nanoindentation model (Surface displacement profiles: spherical indenter).

3.3.3 Flat Punch (Cylindrical) Indenter

Figure 3.7 shows schematic of a flat punch indenter. The indenter has a cylindrical shape and therefore the area of the circle of contact remains the same throughout the indentation.

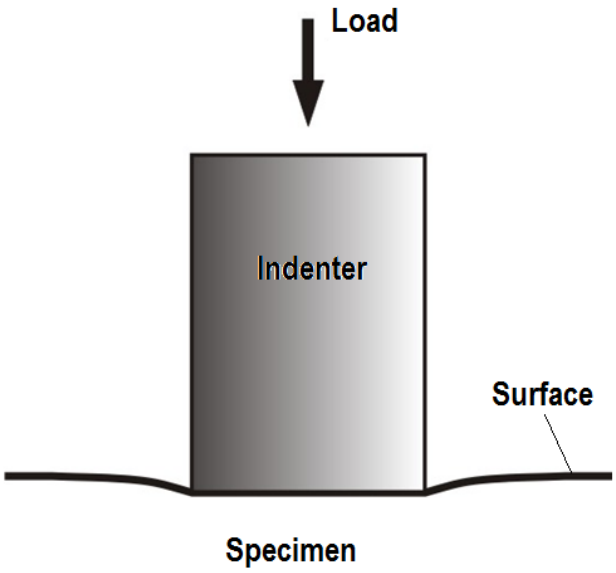

Figure 3.7: Schematic of nanoindentation by the Flat Punch indenter

Area of circle of contact A (i.e. the area of cylindrical tip) is given by:

$$A = \pi a^2 \tag{14}$$

Where a is radius of the cylindrical indenter.

The pressure distribution $p(r)_{cyl}$ is given by [24]:

$$p(r)_{cyl} = p_o \left(1 - \left(\frac{r}{a}\right)^2\right)^{-1/2} \tag{15}$$

Where **r** is the distance from the center of the contact circle and,

$$p_o = \frac{1}{\pi} E^* \frac{h}{a} \tag{16}$$

where h= depth of penetration, E***** = combined modulus of elasticity of the indenter and the specimen.

The indenter load P is given by [24]:

$$P = 2aE^*h \tag{17}$$

To calculate the indention parameters, the following steps were followed:

1. The indenter tip area is calculated by Eq.14 and the ‘n x n’ elements (where n is a positive real number) having area that is nearest to the calculated value is identified.
2. An indenter load is selected and the corresponding value of h is calculated using Eq.17.
3. Now, using Eq.16 and taking E* equal to E (since a rigid indenter is considered) from Eq.6 p_o is calculated.
4. To calculate the pressure on an element within the contact area, the distance from the center of that element to the indenter axis is calculated and recorded as r.

   The maximum pressure is taken to be $3.2P_o$ (that occurs at r = 0.95a). This is because from Eq.15, the pressure approaches infinity as r approaches a, but in practice the edge would not be infinitely sharp for a nanoindenter to cause an infinite pressure [24]. Figure 3.8 shows the pressure distribution beneath the indenter.
5. Now, the pressure on each element is calculated using Eq.15 and applied accordingly.

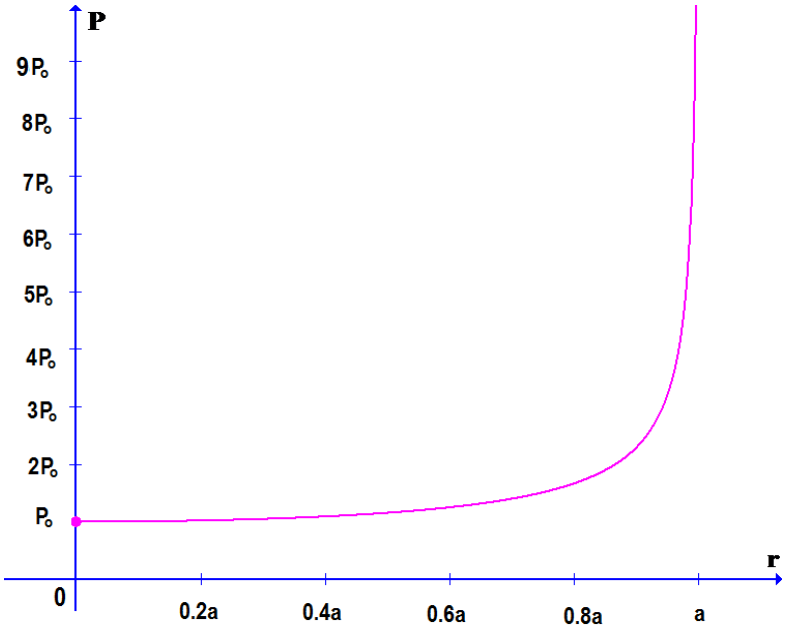

Figure 3.8: Pressure distribution beneath the flat punch indenter.

3.3.4 Conical Indenter

The conical indenter is also commonly used in nanoindentation experiments. Pyramidal indenters such as the Berkovich indenter can also be modeled by converting their geometry to an equivalent cone with an equivalence factor. Figure 3.9 shows the schematic of the conical indenter and Fig. 3.10 shows the significant dimensions of the conical indenter.

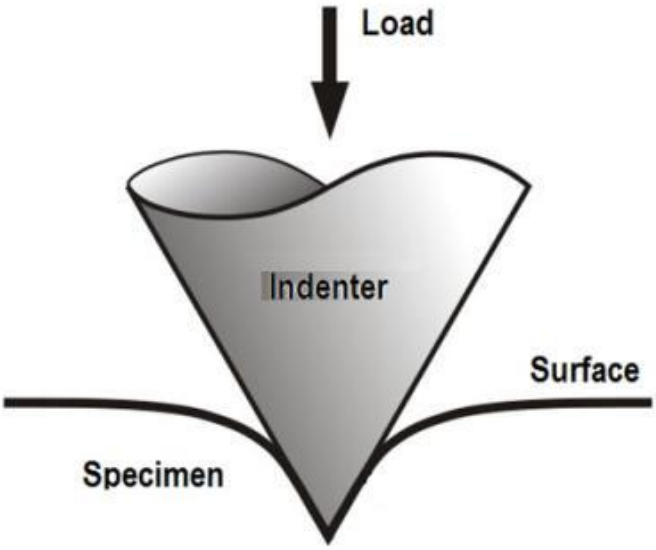

Figure 3.9: Schematic of the conical indenter.

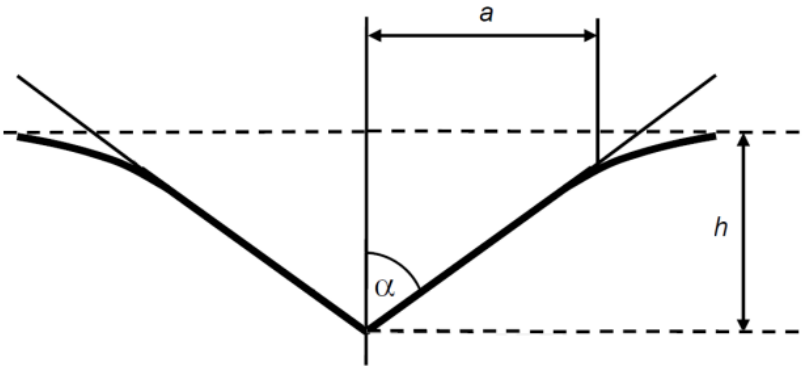

Figure 3.10: Significant dimensions of the conical indenter.

Sneddon's relations [25] are used to calculate the following:

The indenter load P is given by:

$$P = \frac{\pi a}{2} E^{*} a \cot\alpha \qquad (18)$$

The displacement of the specimen surface h(r) is given by:

$$h(r) = \left(\frac{\pi}{2} - \frac{r}{a}\right) a\cot\alpha \quad r \leq a \tag{19}$$

The max displacement h_{max} is given by:

$$h_{max} = \left(\frac{\pi}{2}\right) a\cot\alpha \tag{20}$$

P is related to h(r) by the following relation:

$$P = \frac{2}{\pi} E^* h^2 \tan\alpha \tag{21}$$

The pressure distribution $p(r)_{cone}$ is given by:

$$p(r)_{cone} = \frac{Eh}{\pi a(1-\nu^2)} \ln\left(\frac{a}{r} + \sqrt{\left(\frac{a}{r}\right)^2 - 1}\right) \tag{22}$$

The contact area circle increases as the indenter penetrates the specimen. It can be estimated in a similar manner as it was estimated for the spherical indenter. The contact area is in the form of rectangular elements i.e. 1x1, 3x3 or 5x5 cells and so on. Therefore, it needs to be converted into an equivalent circular area with radius a, to enable the use of Sneddon's relationships.

To calculate the indention parameters, the following steps were followed:

1. The value a is calculated by considering a circle of radius a, with area equivalent to the contact area i.e. by equating both of them.
2. Using the value of a, the indenter load P, is calculated using Eq.18.
3. Now the depth of penetration corresponding to P is calculated using Eq.19.
4. To calculate the pressure on an element within the contact area, the distance from the center of that element to the indenter axis is calculated and recorded as r.

5. Now, the pressure on the element is taken to be $p(r)_{cone}$ and calculated using Eq.22.
6. The pressure approaches infinity (there is a logarithmic singularity of the stress) at the tip of the cone. In practice, an indenter would not have an infinitely sharp tip radius. So, the maximum pressure is considered to be equal to $3.7\frac{Eh}{\pi a(1-\nu^2)}$ (at r = 0.05a) for simplicity. Figure 3.11 shows the pressure distribution beneath the conical indenter.
7. The pressure is applied in ten increments in ten consecutive creep time steps.
8. Steps 1-7 are repeated once the indentation progresses from 1x1 elements to 3x3 and again for 5x5 elements.

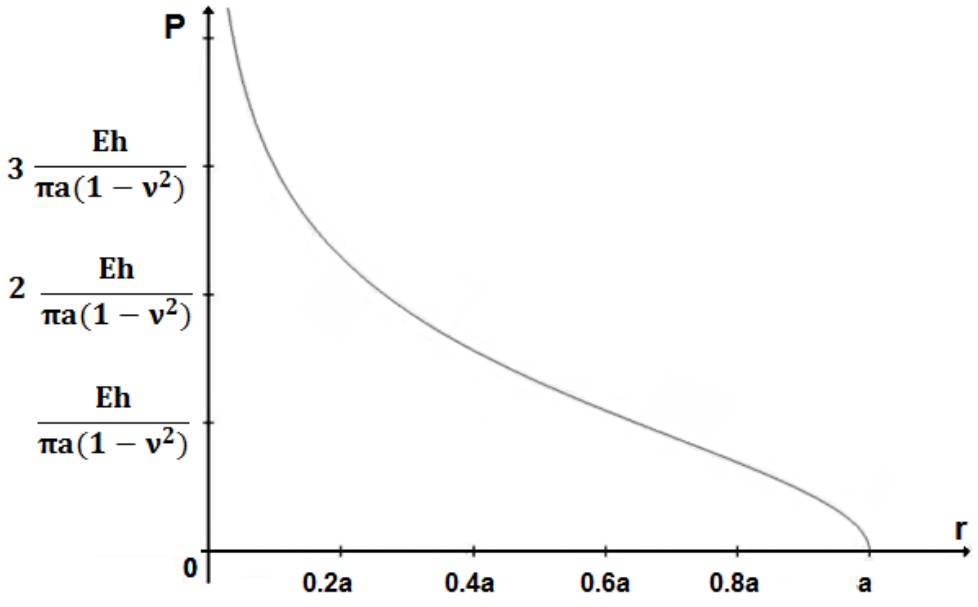

Figure 3.11: Pressure distribution beneath a conical indenter.

3.3.5 Berkovich Indentor

The Berkovick indenter can be analyzed in terms of an equivalent conical indenter by a suitable equivalence factor [24]. The contact area A is given by.

$$A = 3\sqrt{3}h^2\tan^2\theta \tag{23}$$

Where h is the depth of indentation and θ is the characteristic angle.

But $\theta = 65.3^o$ for Berkovich indenter, hence

$$A = 24.49h^2 \tag{24}$$

The equivalent cone angle α is equal to 70.296^o for a Berkovich indenter [24].

The subsequent process and equations are the same as those applied to the conical indenter.

3.4 Frank Read Sources

MDDP cannot simulate nucleation of dislocations and requires initial dislocations to be present in the simulation cell. Various distributions, random and from atomistic simulations, of Frank-Read Sources (FRS) were used for the simulations.

FRS are placed in pairs in parallel slip planes to form a continuous dislocation source loop. Each pair consists of oppositely signed FRS (i.e. having the same Burgers vector but opposite line sense). It is defined by a set of four nodes that are pinned onto their specified locations. The coordinates, interconnectivity and Burgers vectors of these nodes is defined in the file "*DD*input". The average length of an FRS is 1100 **b** (where **b** is the

magnitude of Burgers vector). Three different configurations of dislocation source were considered:

1. **Configuration 1**: FRS are randomly placed throughout the simulation cell. Figure 3.12 shows the initial random configuration of FRS in the crystal.

2. **Configuration 2:** Only three FRS are placed just beneath the top surface, around the indentation axis to model the dislocation configuration at the end of an atomistic simulation [32] (Fig. 3.13). One FRS is placed each on a different type of slip plane that intersect the horizontal surface.
3. **Configuration 3**: FRS loops are placed only on one type of slip planes (the (111) planes) at regular intervals (details are provided in section 3.6).

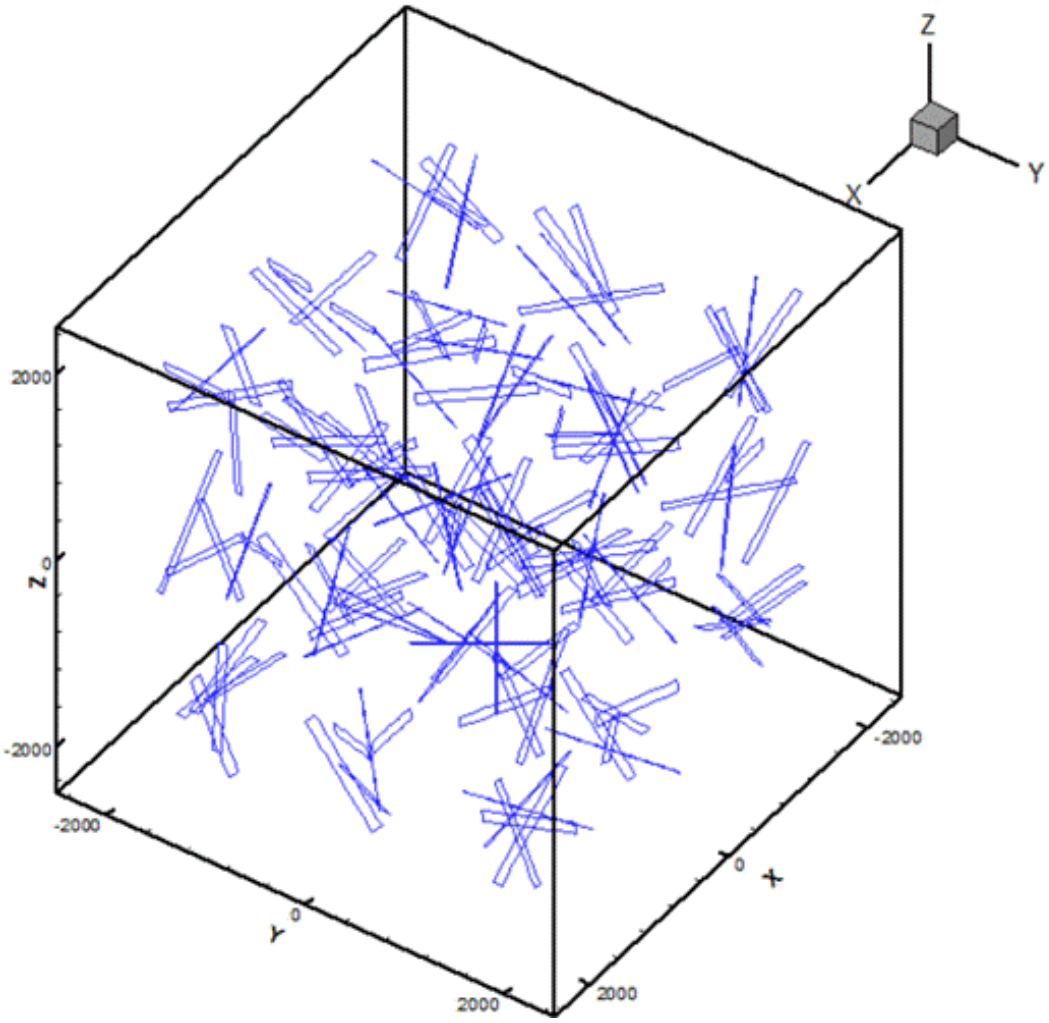

Figure 3.12: FRS configuration 1 (Units are in Burgers vector).

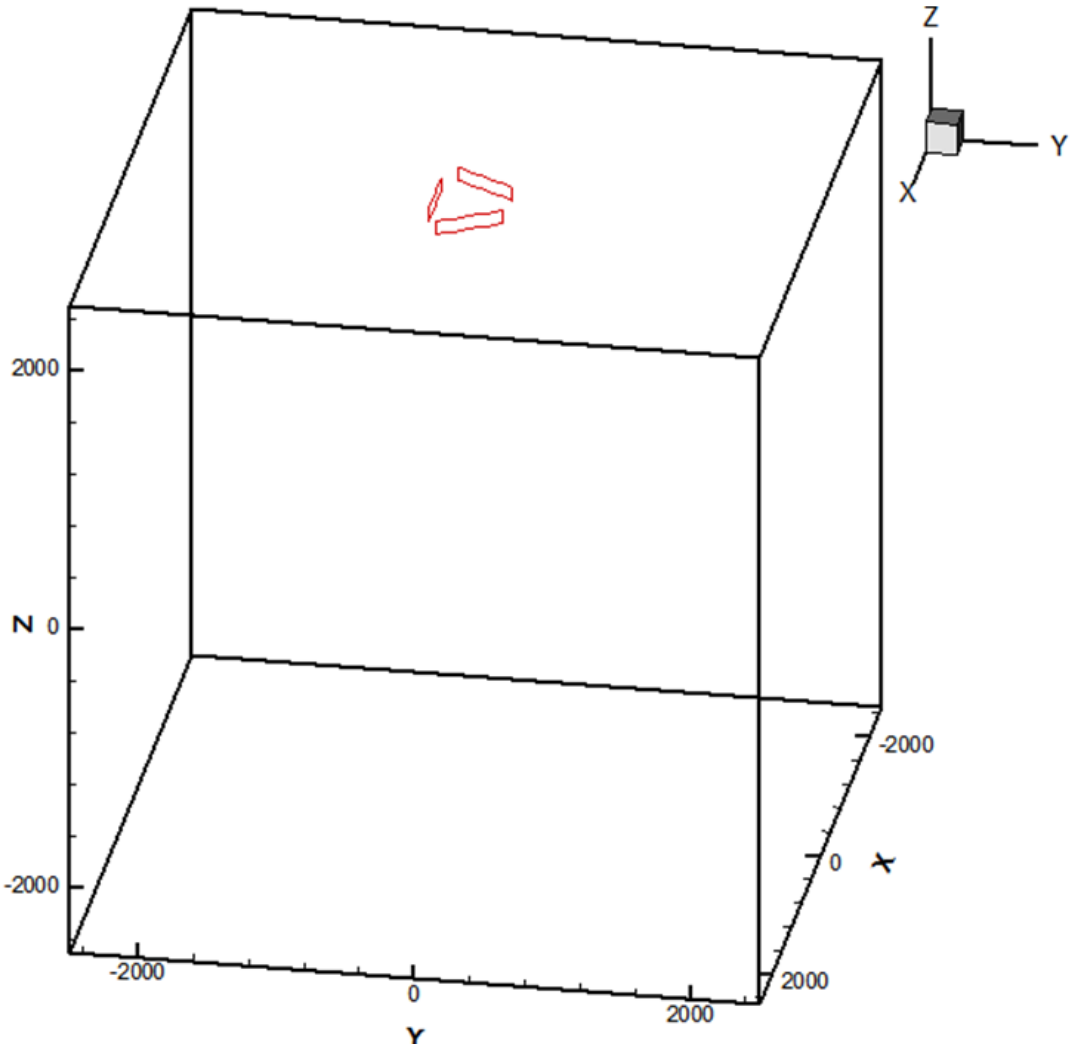

Figure 3.13: FRS configuration 2b (Units are in Burgers vector).

3.5 Setups to Simulate Nanoindention

Simulations were carried out for different indenter types, dislocation configurations and orientation of the crystal. Table.3.1. summarizes the setups for nanoindentation simulations.

Table 3.1: The setups for nanoindentation simulations.

Setup	Configuration of dislocation sources	Indenter type	RVE Top surface orientation
1	Configuration 1	Spherical (radius = 230 nm)	[111]
2	Configuration 2	Spherical (radius = 230 nm)	[111]
3	Configuration 1	Spherical (radius = 230 nm)	[001]
4	Configuration 2	Spherical (radius = 230 nm)	[001]
5	Configuration 1	Berkovich (Angle= 65.3^{o})	[111]
6	Configuration 2	Berkovich (Angle= 65.3^{o})	[111]
7	Configuration 3	Spherical (radius = 230 nm)	[001]
8	Configuration 3	Spherical (radius = 400 nm)	[001]

3.5.1 Input Parameters

The material selected was single crystal, pure gold with FCC structure [30]. It had a density of 19,300 (kg/m^3), shear modulus of 27 GPa and Poissons ratio equal to 0.44. The dislocation mobility was 1000 Pa/s and the magnitude of Burgers vector was 0.2884 nm. The dimensions of the crystal (computational cell) were: 1.44 μm x 1.44 μm x 1.44 μm.

3.6 Set up to investigate 2D models

To investigate the accuracy of nanoindentation size effect model developed based on 2D simulations, FRS loops are placed only on one type of slip planes (the (111) planes) at regular intervals in a similar way to that in the 2D model by Kruezer and Pippan [4, 26-28], as shown in Fig. 3.14.

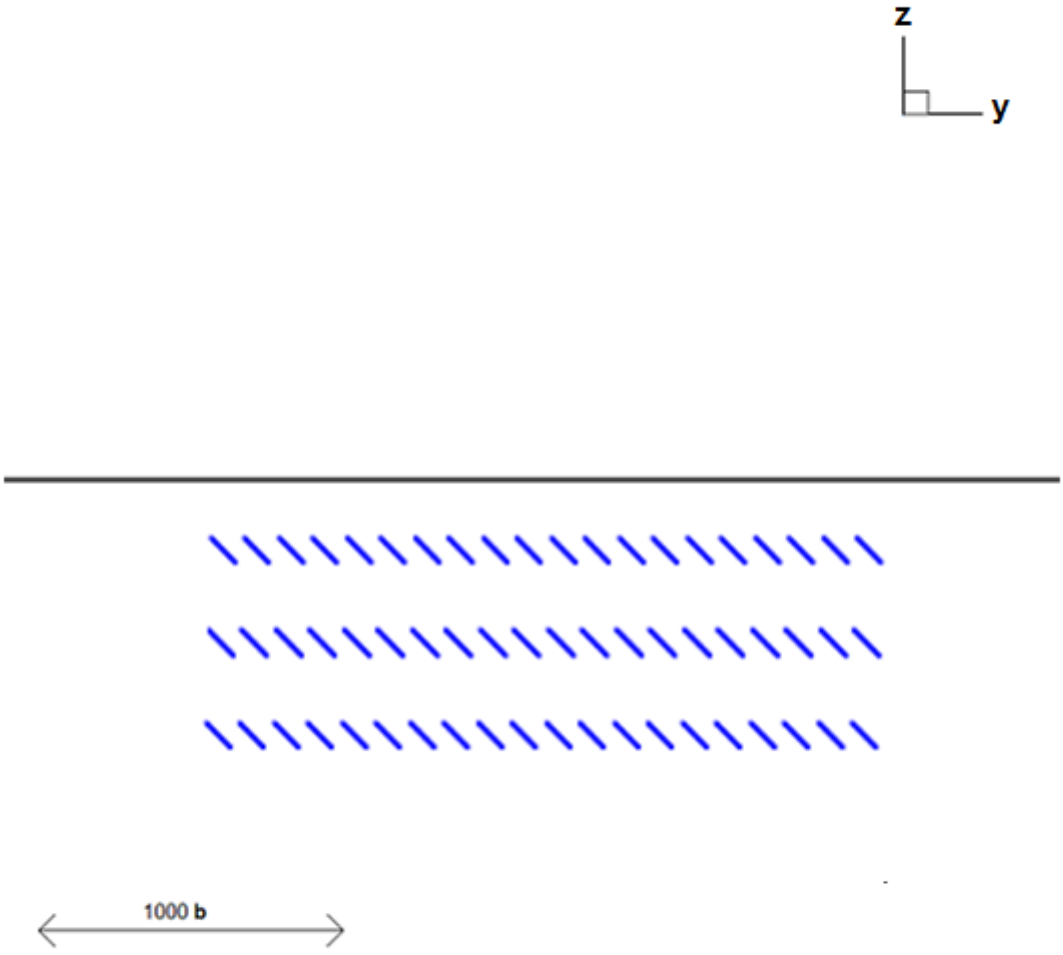

Figure 3.14: Initial setup of FRS to investigate 2D nanoindentation models.

3.7 Topographic map of Nanoindented surface

Topographic maps of nanoindented surface are three dimensional maps that show material displacement in the vicinity of the nanoindenter. They are useful in relating the patterns of slip steps (formed due to material displacement) to the crystal orientation and the initial dislocation configuration. Dislocations exit the top surface of the crystal during nanoindentation and leave behind slip steps on that surface [31]. A subroutine in *MDDP*, writes the coordinates and vectors of the exiting dislocation segments as soon as they exit the top surface. The data is recorded in an output file (named "sgtecplotesc.out"). Each exiting line segment raises the surrounding surface by a magnitude of one Burgers vector.

A program is created in Microsoft® Excel® to generate topographical map of nanoindented surface based on exiting dislocations.

The following procedure was followed:

1. The coordinates and vectors defining the exiting dislocation segments are read from the file sgtecplotesc.out.
2. The length of each segment is calculated and recorded.
3. Linear interpolation method is used to divide each line segment into sub segments of equal length. The program automatically adjusts the number of sub segments according to the length of the segment.
4. The coordinates of the end points (nodes) of all the sub segments are recorded.
5. An area of 2000**b** X 2000**b** on the center of the top surface is chosen. This is the area of interest because most of the dislocations exit through this area.

6. This chosen area is divided into 40,000 small square elements (each with a side dimension of 10b) using a fine mesh.
7. Now a statistical code counts for each element, the number of times a dislocation segment has crossed this element. It does this by counting the total number of sub segment points that reside in that element. This value is recorded as the "z" value.
8. A 3D surface chart is plotted, using the **x**, **y** values as **x** and **y** coordinates of the mid-point of the grid elements and the **z** value from step 7.

CHAPTER 4

RESULTS

4.1 Dislocation Evolution

Nanoindentation simulations were carried out with spherical indenter of tip radius 230nm on crystals with two different orientations, [001] and [111]. FRS configuration 1 was used. Figure 4.1 shows the dislocation structure evolution during nanoindentation for setup 1 (FRS configuration 1, [111] RVE orientation, 230nm spherical indenter) and Fig. 4.2 shows the dislocation structure evolution for setup 3 (FRS configuration 3, [001] RVE orientation, 230nm spherical indenter). Low cross-slip activity was observed as the indentation progressed and the dislocation density began to increase. Dislocations were observed to exit the top surface mostly from the slip planes where a random FRS was initially present. Figures 4.3 & 4.4 show the patterns of dislocations exiting the top surface for the setup 1 and 3 simulations respectively. The patterns were observed to be irregular, scattered and unsymmetrical. Repeating the simulations after re-randomizing the positions of FRS for FRS configuration 1 produced similar results. The dislocation activity was higher on the slip planes where a random FRS was present initially. Therefore, it can be concluded that the dislocation evolution was concentrated around the indentation location especially near the top surface. However, there was considerable expansion of dislocation loops below and around the indentation region. Therefore, the shape of the region where the GNDs reside was not well defined. There

was a high dislocation activity within this region only in those slip planes where a random FRS was present.

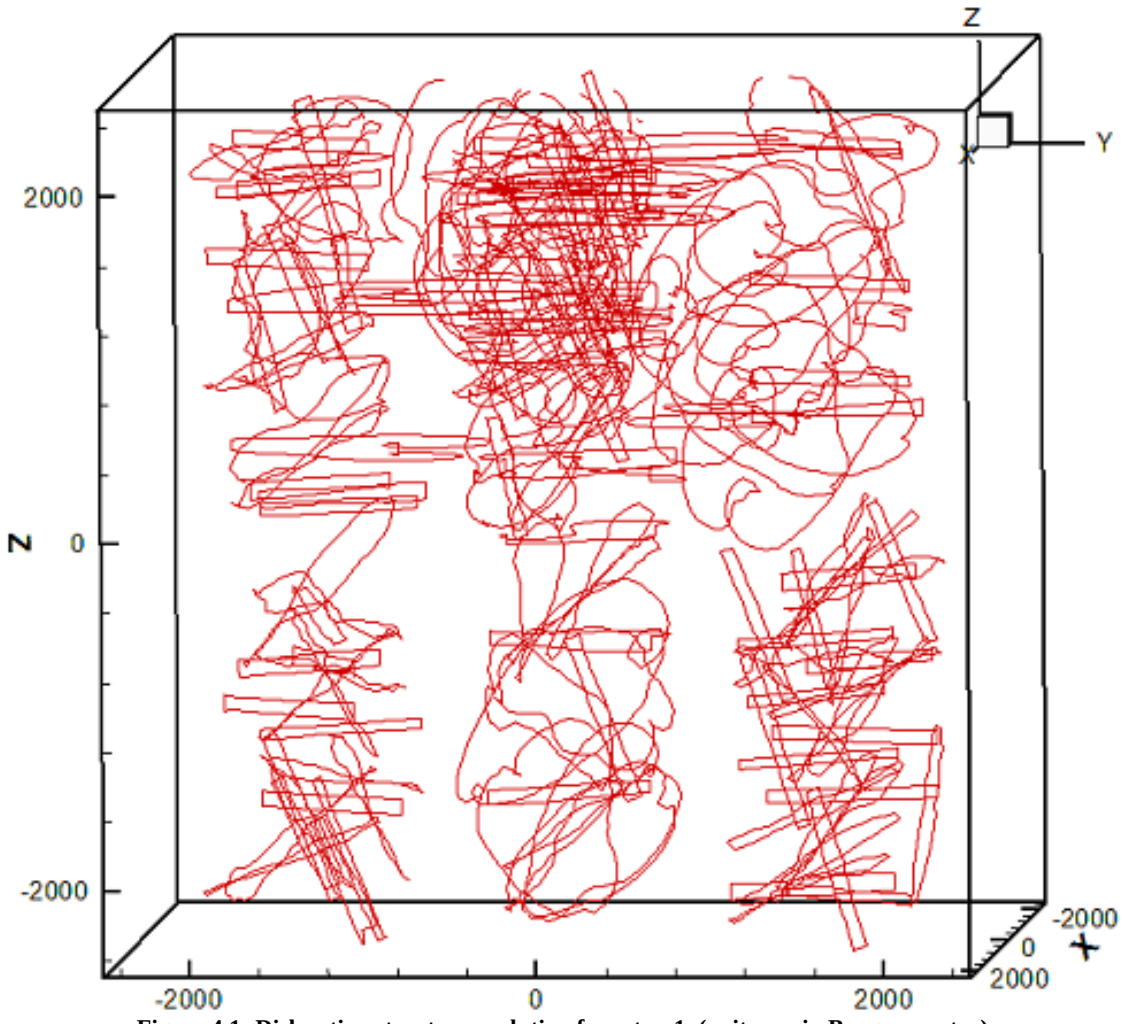

Figure 4.1: Dislocation structure evolution for setup 1. (units are in Burgers vector).

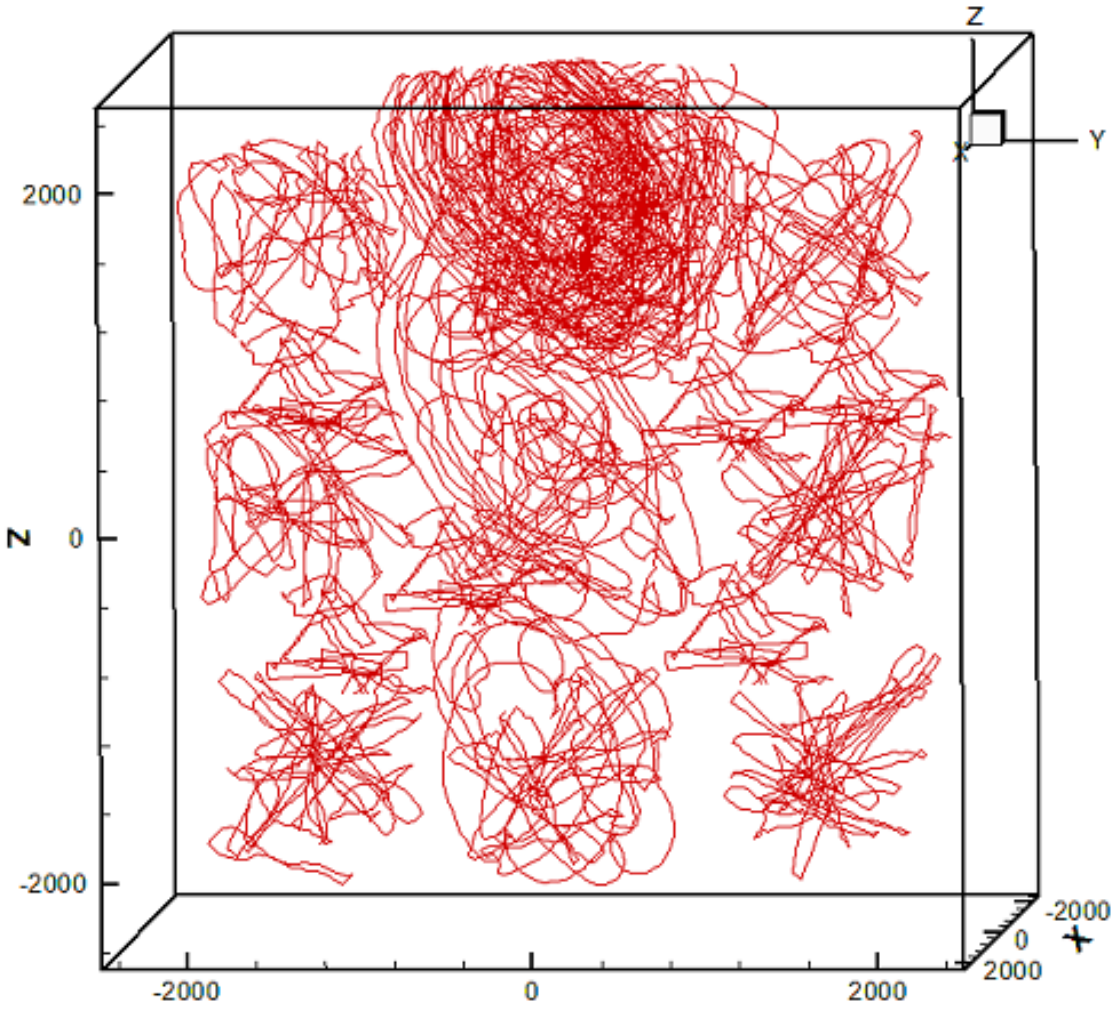

Figure 4.2: Dislocation structure evolution for setup 3. (units are in Burgers vector).

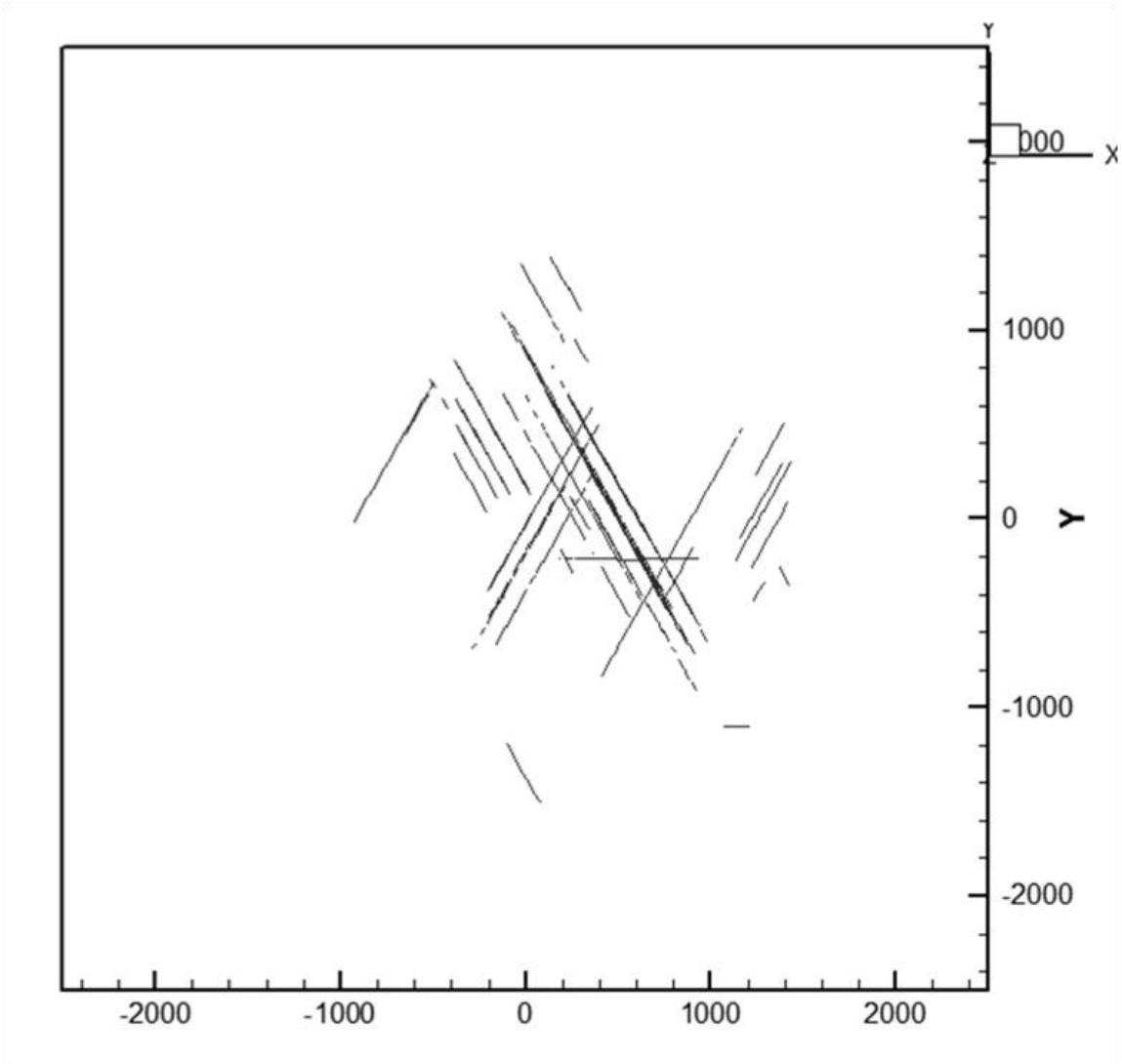

Figure 4.3: The pattern of dislocations exiting the top surface for setup 1. (units are in Burgers vector).

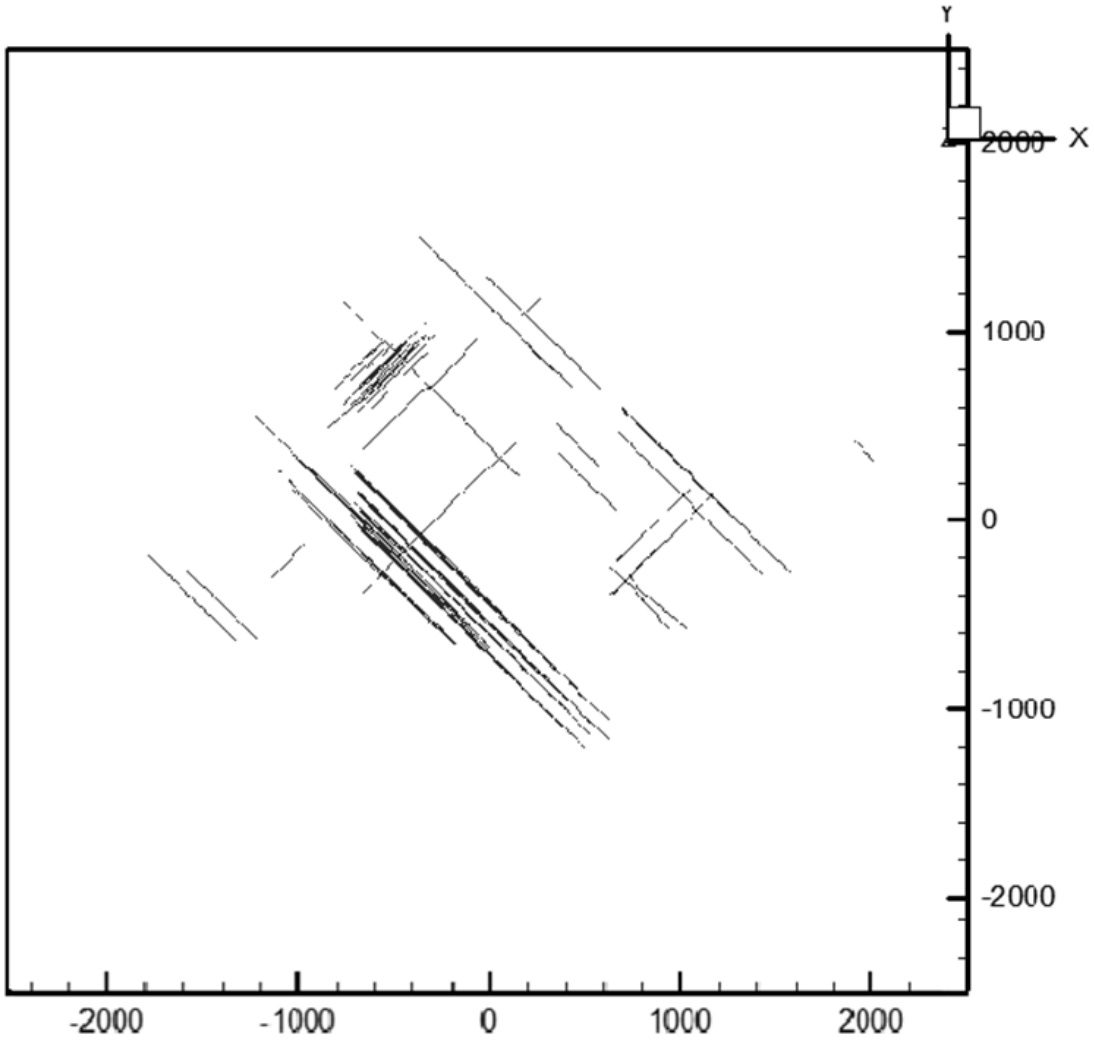

Figure 4.4: The pattern of dislocations exiting the top surface for setup 3. (units are in Burgers vector).

Nanoindentation simulations were also carried out with spherical indenter of radius 230nm on crystals with orientation [001] and [111] and FRS configuration 2 (setup 4 and 2 respectively). It was observed at the beginning of the simulation, in both cases, that the dislocation sources generated dislocation loops that expanded on their respective slip planes towards the top surface and into the crystal. Most of the dislocation activity was observed just beneath the indenter tip. The dislocation evolution was restricted to a region within and around the indentation zone (i.e., in a circle of radius 0.3 μm around the

indentation and 0.3 μm below it). There was high dislocation activity on all {111} planes. The volume distribution of GND approximately had the shape of a hemisphere. Figure 4.5 shows the dislocation structure evolution for setup 4 and Fig. 4.6 shows the dislocation structure evolution for setup 2. Significantly more cross-slip (compared to the simulation with FRS configuration 1 while keeping other setup the same) activity was observed as the indentation progressed and the dislocation density began to increase. The dislocations initially exiting the top surface belonged to the slip planes closer to the indentation location. Later, the dislocations began to exit the top surface from the slip planes that were further away from the indentation location inside the RVE. Figure 4.7 shows the patterns of dislocations exiting the top surface during nanoindentation for setup 4 and Fig. 4.8 shows the patterns for setup 2. The patterns are regular and symmetric and depend on the orientation of the slip planes with respect to the top surface. Moreover, these patterns have higher dislocation density compared to the simulation with FRS configuration 1 (setup 1 & 3) because of a greater increase in dislocation density in the nanoindentation zone (as discussed in section 4.2)

The highest concentration of dislocations exit closer to the indentation site and this intensity gradually decreases outwards. This is because the dislocation activity is highest on the slip planes closer to nanoindentation zone and it decreases progressively to distant slip planes. Repeating these simulations for FRS configuration 2 produced similar results of dislocation activity and showed that the patterns of exiting dislocations are repeatable.

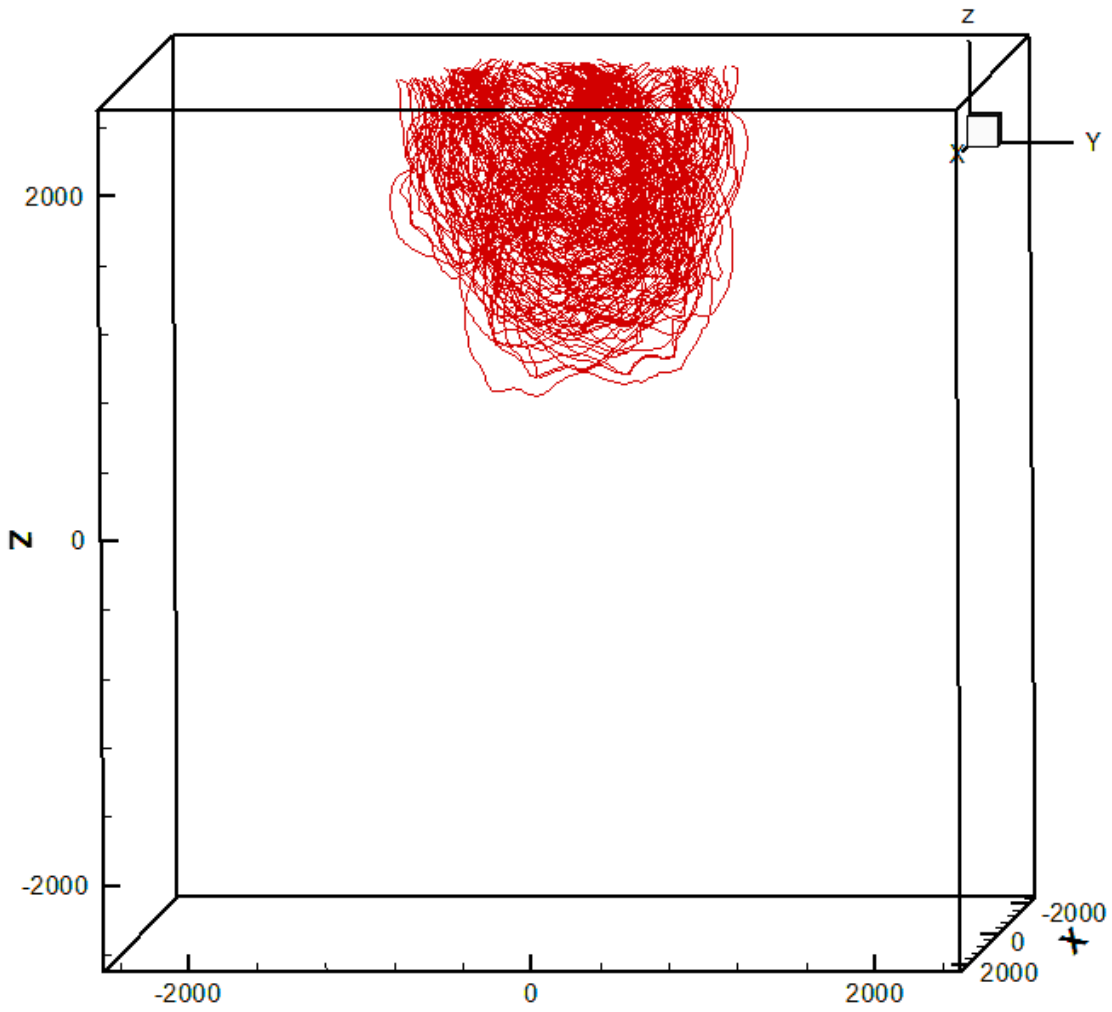

Figure 4.5: Dislocation structure evolution for setup 4 (units are in Burgers vector).

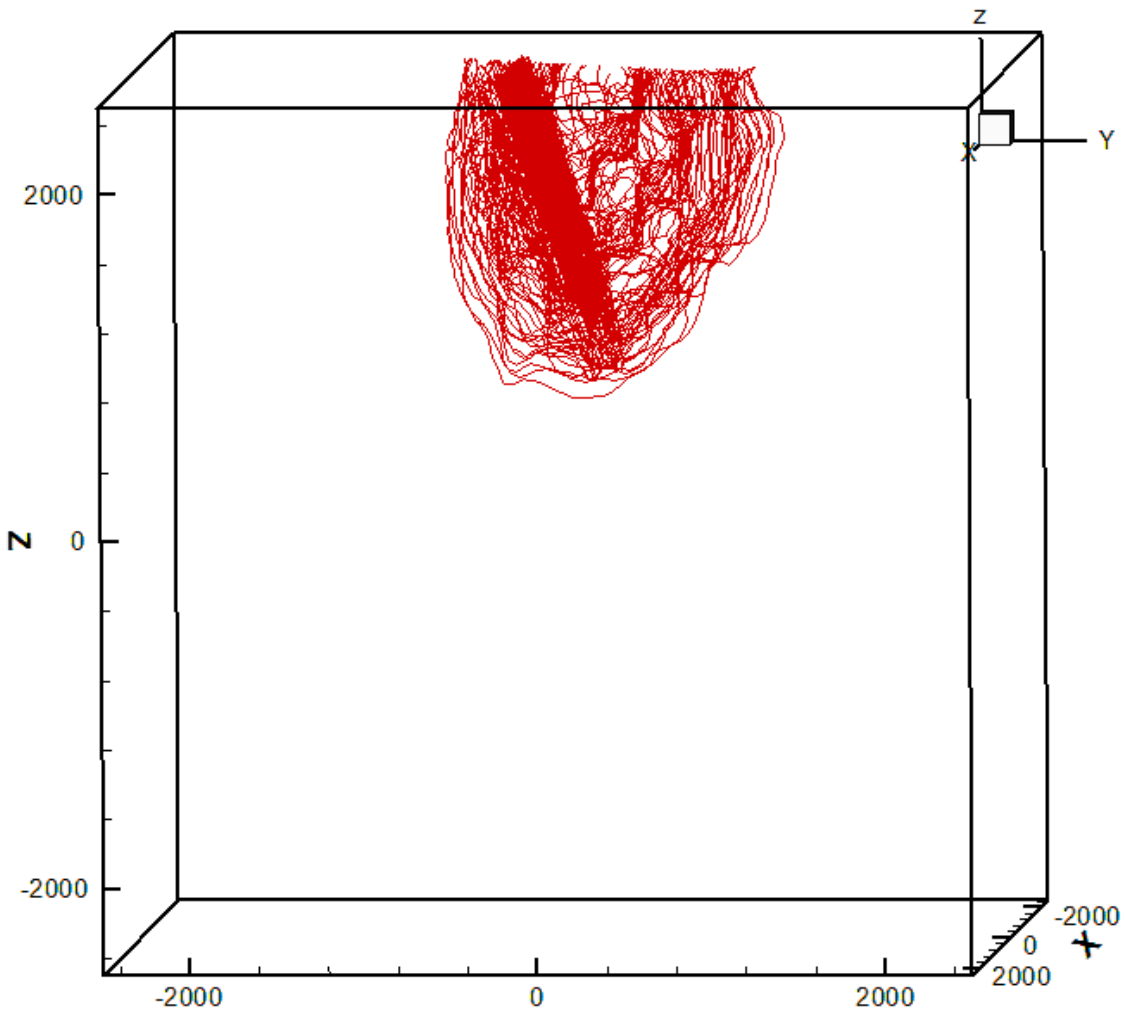

Figure 4.6: Dislocation structure evolution for setup 2 (units are in Burgers vector).

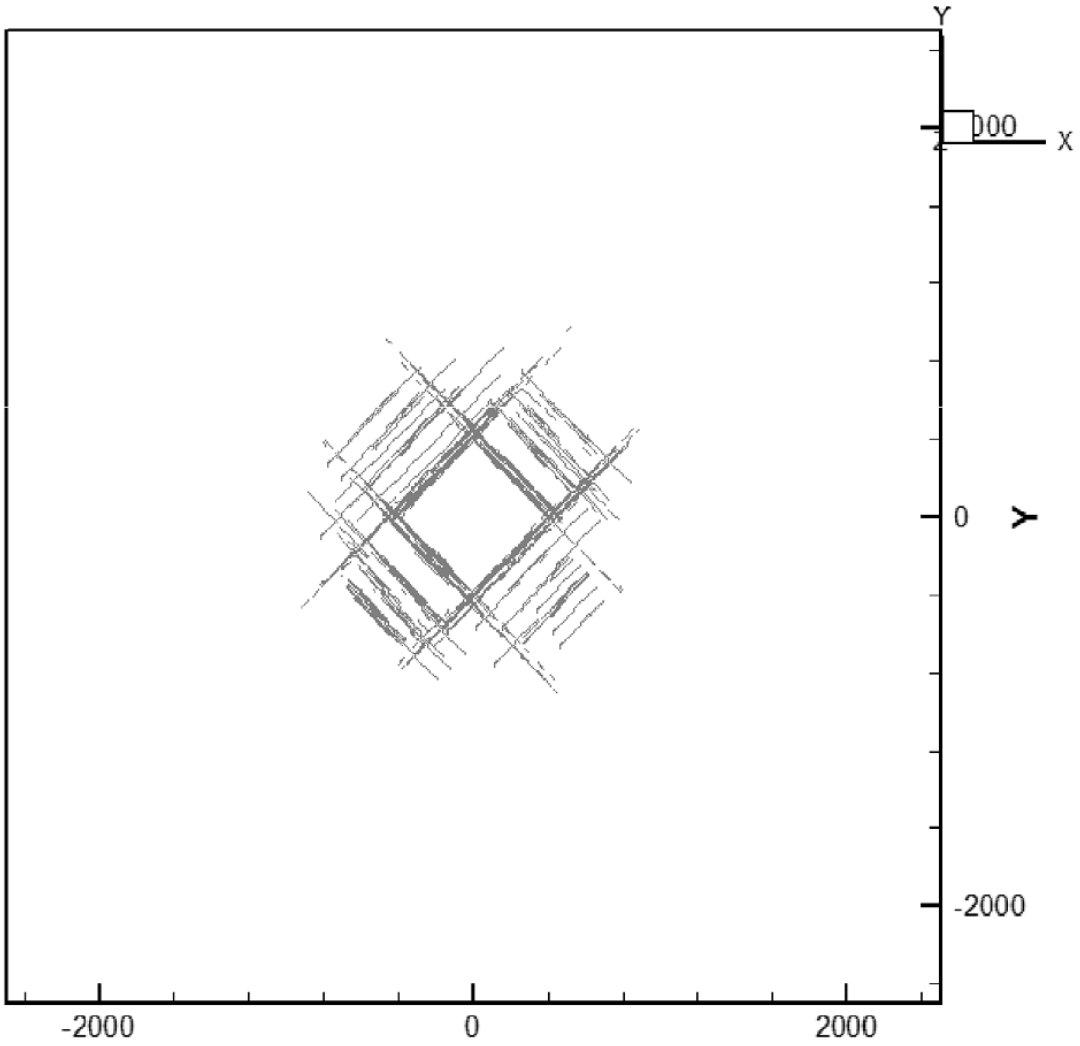

Figure 4.7: Dislocation structure evolution for setup 4 (units are in Burgers vector).

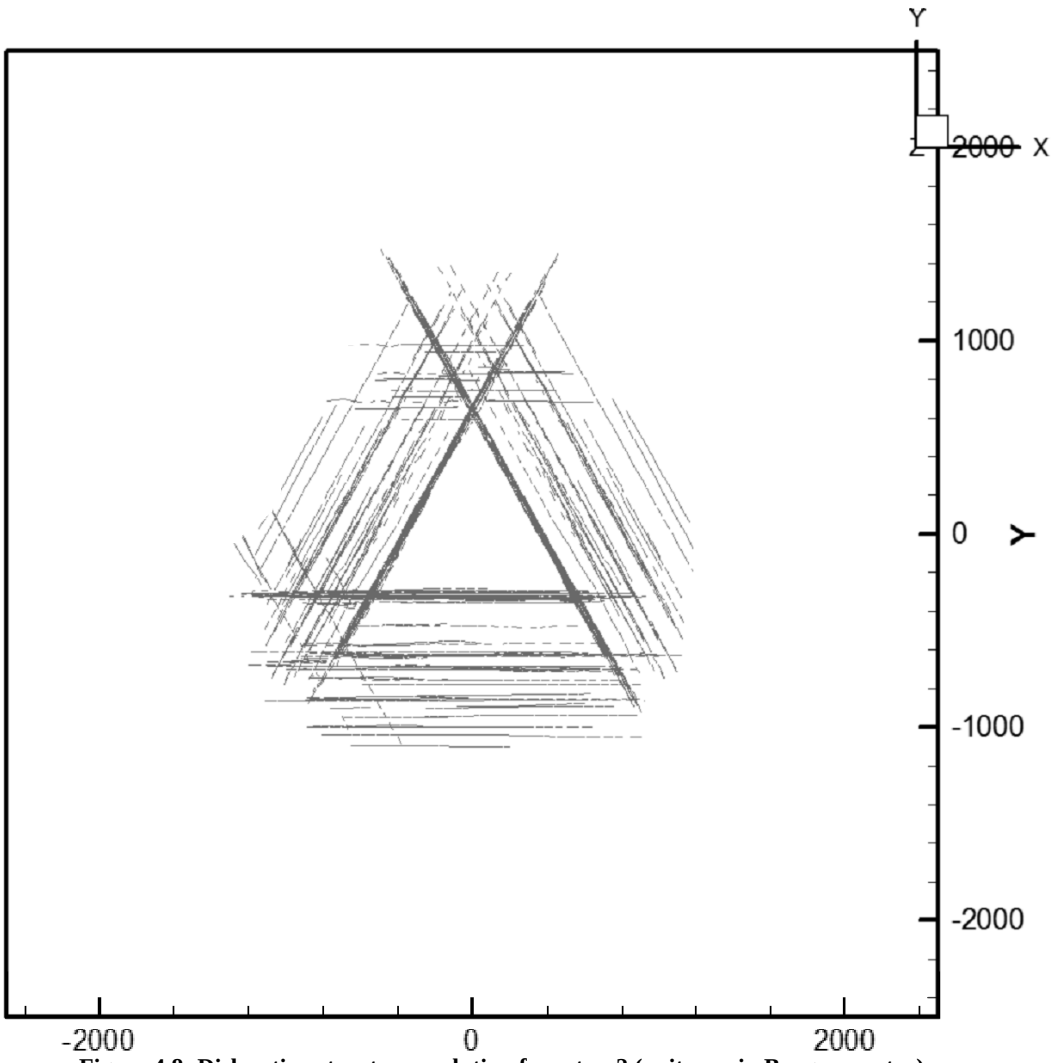

Figure 4.8: Dislocation structure evolution for setup 2 (units are in Burgers vector).

4.2 Dislocation Density

Figure 4.9 and 4.10 show the plots of dislocation density verses the applied indenter load for [111] and [001] crystal orientations respectively (setups 1-4). It can be clearly seen that the simulations with the FRS configuration 2 show a significant rise in the dislocation density compared to the simulations with the FRS configuration 1. This

enormous difference is similar for both the crystal orientations. Table 4.1 compares the percentage increase in dislocation density at the end of the simulations. This huge difference in the dislocation densities is due to significantly more dislocation multiplication in the vicinity of the indenter (in the case of FRS configuration 2). This is because the FRS in this case, are located in the region where the highest nanoindentation pressure is applied.

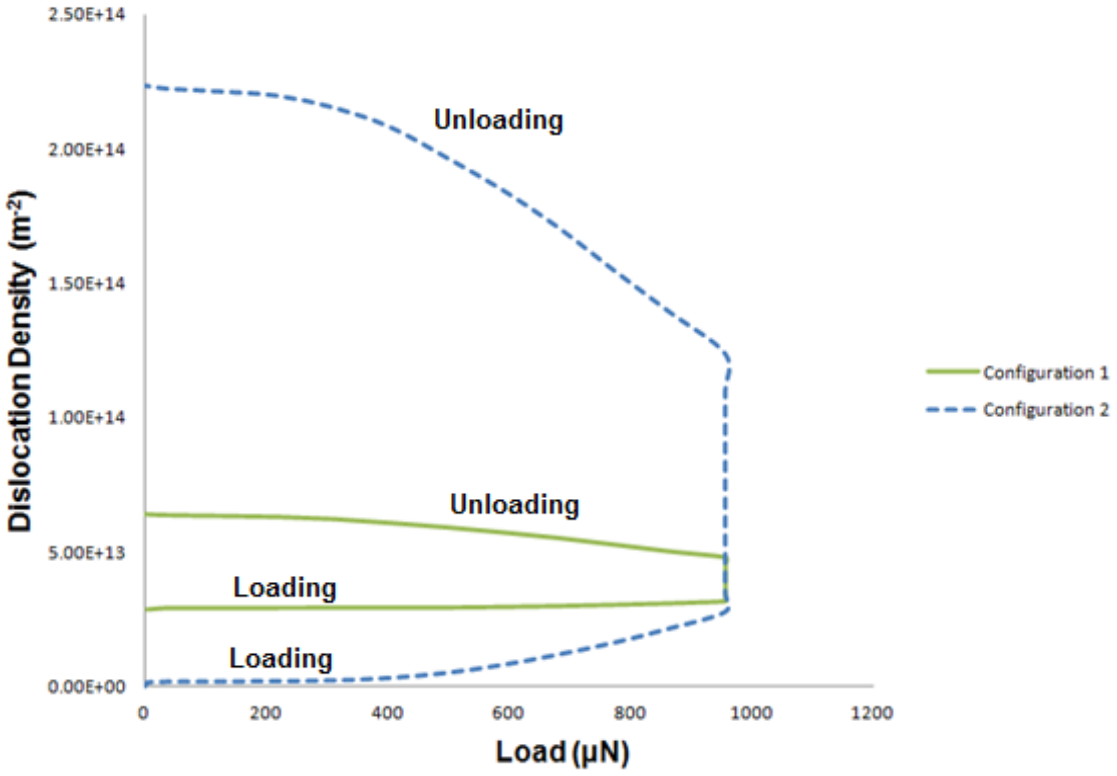

Figure 4.9: Dislocation density variation with applied load during nanoindentation for [111] crystal orientation (setup 1 & 2).

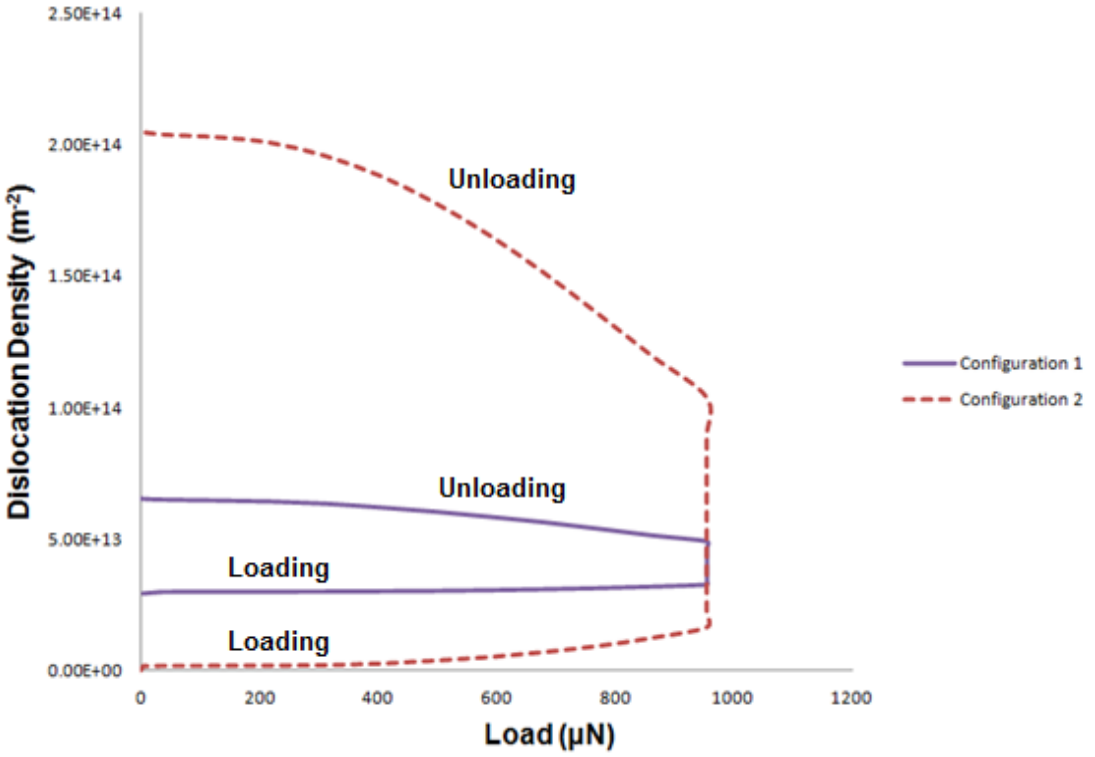

Figure 4.10: Dislocation density variation with applied load during nanoindentation for [001] crystal orientation (setup 3 & 4).

Table 4.1: Comparison of percentage increase in dislocation density for different crystal orientations at the end of nanoindentaion with spherical nanoindenter (radius = 230nm).

Configuration	Crystal Orientation	% increase in Dislocation Density
1	[111]	15,858
2	[111]	122
1	[001]	13,190
2	[001]	124

4.3 Topographical Maps of Nanoindented Surfaces

The topographic maps of the nanoindented surface were generated using the computer program described in the previous chapter. An exiting dislocation segment raises the surface by the magnitude of the Burgers vector at the exit site. Therefore, if more dislocation segments exit at a particular location then it will have a higher elevation in the surface. The slip steps, formed at these locations, had regular and symmetric patterns for simulations with FRS configuration 2 (Fig. 4.11 and Fig. 4.12) and random and nonsymmetric for simulations with FRS configuration 1 (Fig. 4.13 and Fig. 4.14).

Most slip steps were confined to an area of radius **0.3** μm around the indentation location. For FRS configuration 2 the slips steps progressively reduced in height and length away from the indentation axis. The step height was greater on locations where there was more dislocation exit and vice-versa. The average height of the slip steps near the indentation axis was 6.1nm for [001] crystal orientation and 7.2nm for [111] crystal orientation. For FRS configuration 1 the slips steps were found to be situated randomly near the indentation axis and had heights varying from 0.6nm to 1.5nm. This was because of the randomness of dislocation exit patterns (as discussed in section 4.1). Repeating the simulations for FRS configuration 2 with a spherical indenter of radius of 400nm, showed a similar pattern.

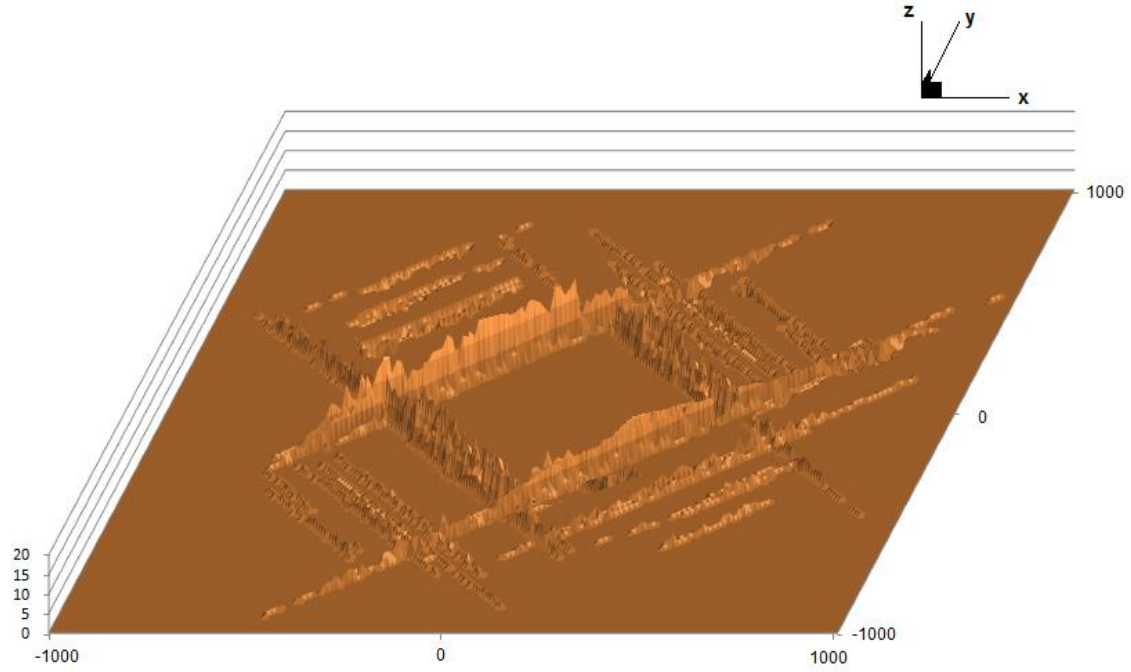

Figure 4.11: Topographic map of the nanoindented surface for setup 4 (units are in Burgers vector).

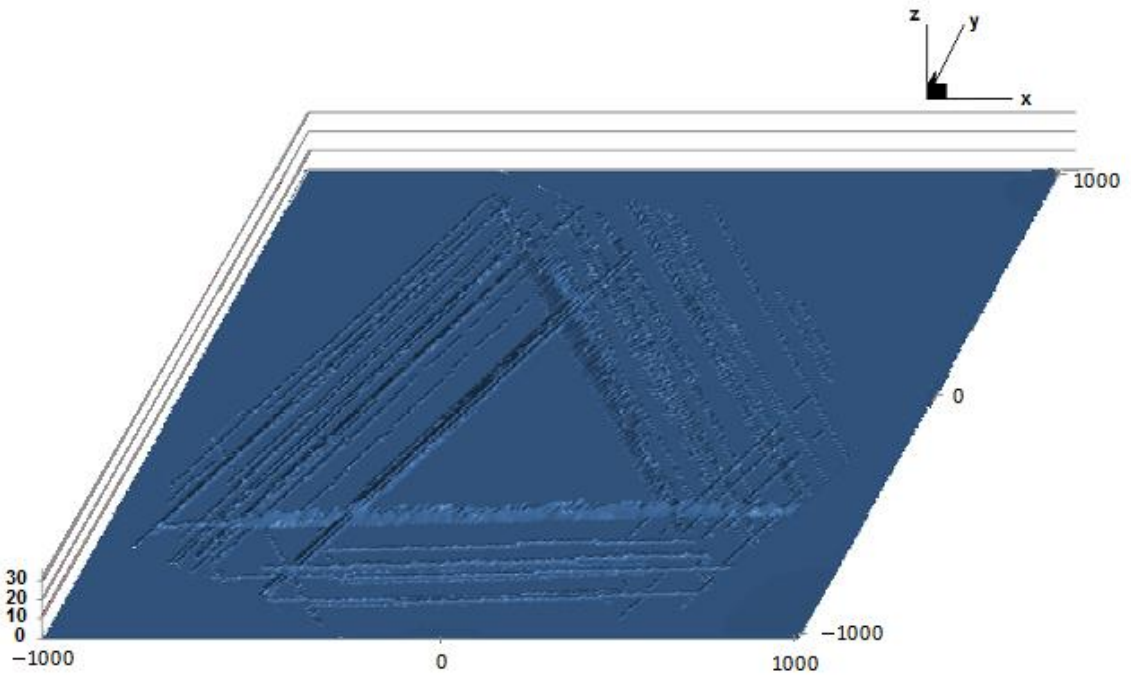

Figure 4.12: Topographic map of the nanoindented surface for setup 2 (units are in Burgers vector).

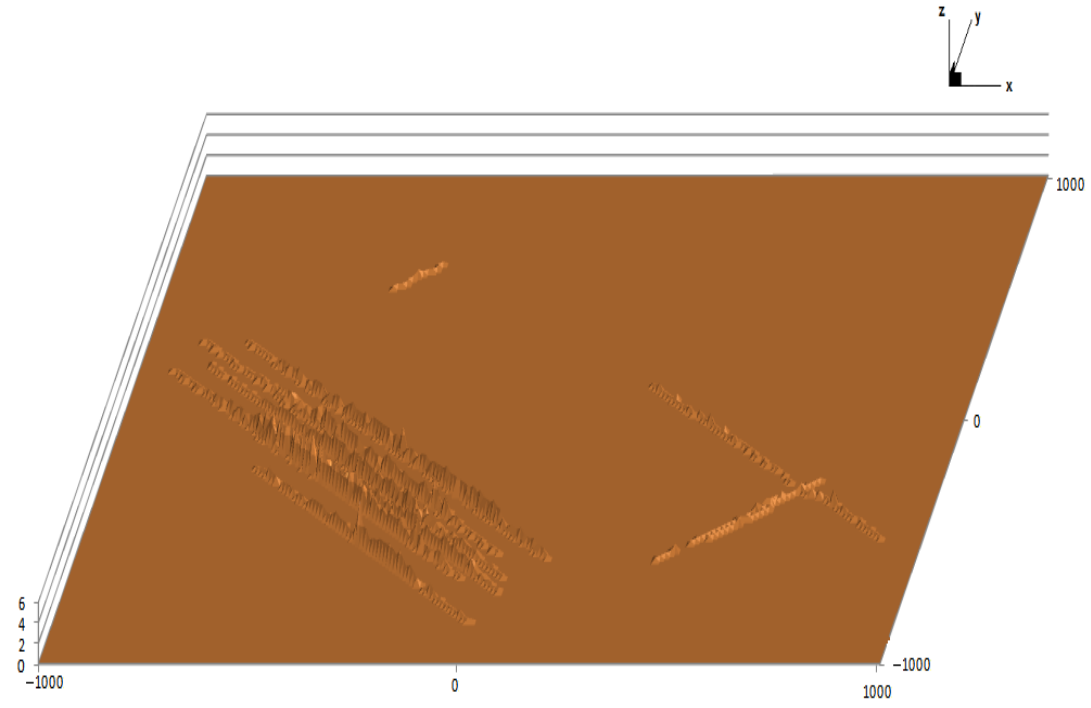

Figure 4.13: Topographic map of the nanoindented surface for setup 1 (units are in Burgers vector).

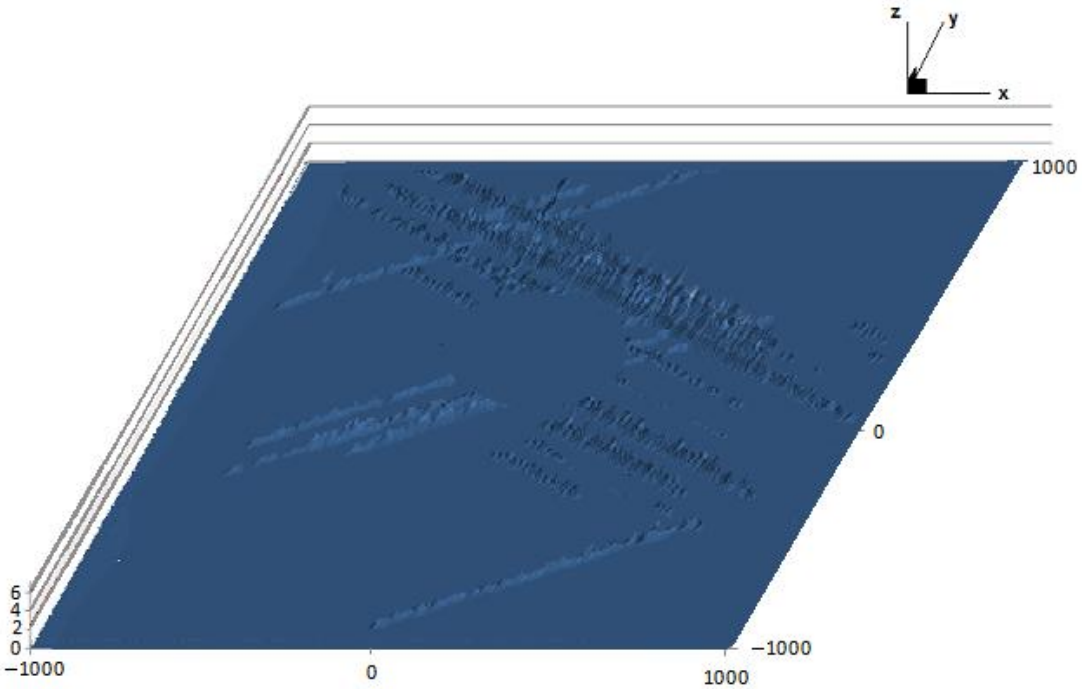

Figure 4.14: Topographic map of the nanoindented surface for setup 3 (units are in Burgers vector).

The patterns of slip steps in simulations with FRS configuration 2 showed symmetry and trend of decrease in slip step height, consistent with atomic force microscopy observations of nanoindentation by Nibur and Bahr [31]. Therefore, dislocation activity in simulations with FRS configuration from the atomistic simulations results in a better and uniform topography compared to simulations with random FRS configuration.

4.4 Cross-Slip and Hardness

Simulations were carried out for FRS configuration 3 with a spherical nanoindenter of radius 400nm to investigate the effect of cross-slip on the hardness verses displacement behavior and to compare it with the results of 2D models [26-29]. The 2D models do not consider intersecting planes and therefore fail to consider cross-slip. The hardness verses indentation depth graphs are initially very steep and as the indentation depth increases, their steepness decreases considerably to achieve a plateau.

Initially the FRS began to generate dislocation loops, which expanded on their respective glide planes (Stage 1: Fig. 4.15) as in the 2D models [8-10]. However, it was noted that as soon as the dislocation density on these planes increased, the dislocations began to cross slip to other {111} type slip planes and were again free to expand (Stage 2: Fig. 4.16). Therefore, the increase in hardness with increasing depth of indentation is expected to be lower, compared to the 2D models. With time, the dislocation density on the cross-slipped planes increased considerably (Stage 3: Fig. 4.17). Dislocation jogs were formed generating FRS on the cross- slipped planes. At this stage, the hardness is noted to

increase more in the 3D model since there is strong interference on glide motion between dislocations on intersecting planes (this phenomenon is referred to as strain hardening). The hardness verses indentation graph for 3D simulations (Fig. 4.18) shows that the initial increase in hardness is not as steep as in the 2D models and the slope of the curve decreases gradually but not to the same extent as those of 2D models. Therefore, it is obvious that the cross-slip mechanism affects hardness and the indentation size effect.

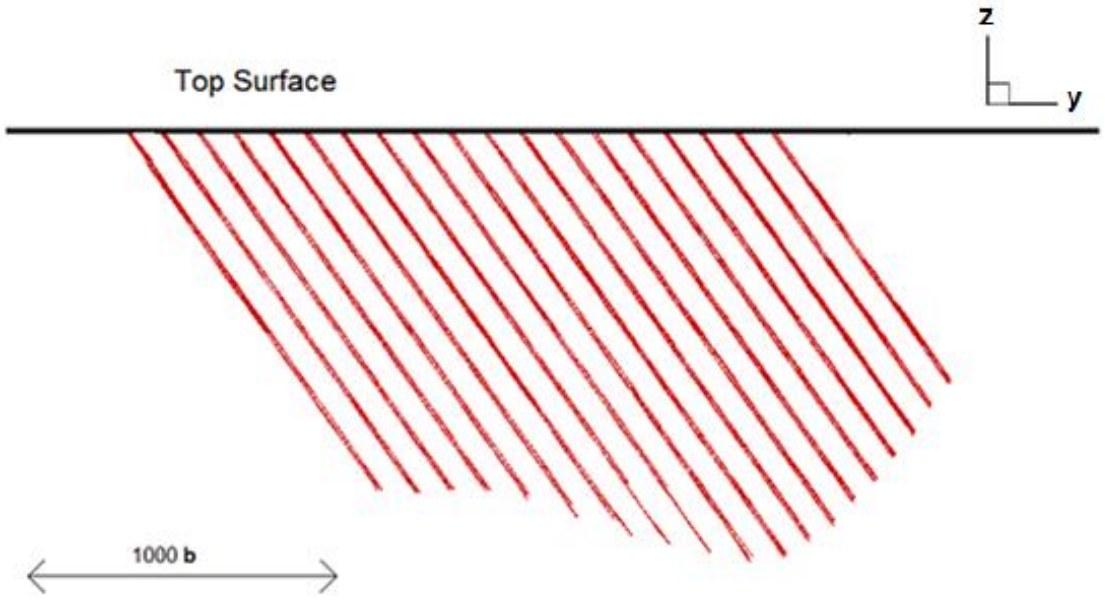

Figure 4.15: Dislocation structure evolution during nanoindentation with initial FRS configuration 3; Stage 1.

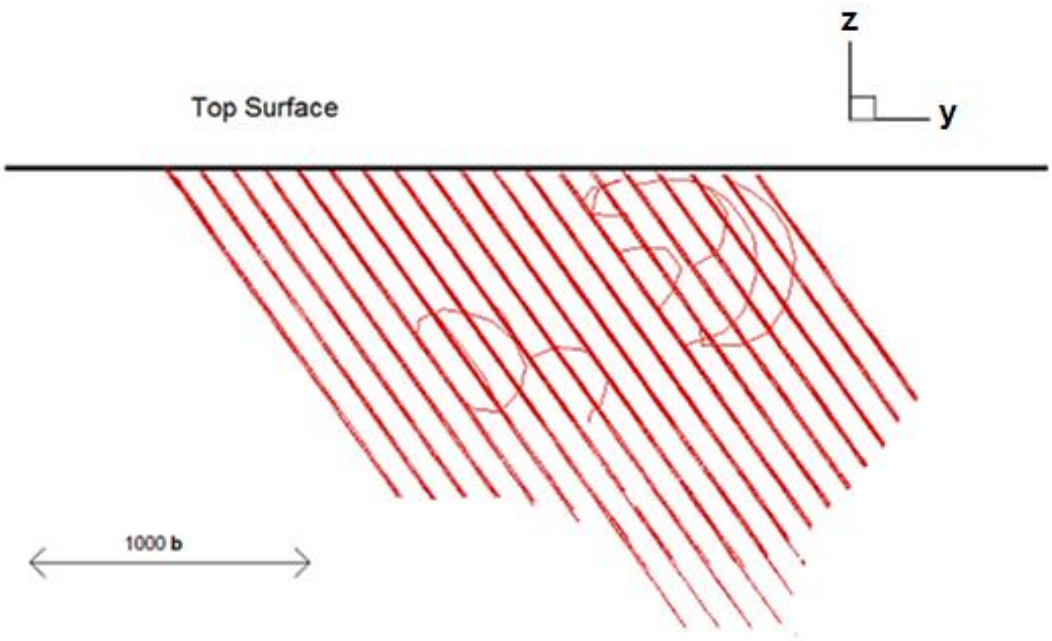

Figure 4.16: Dislocation structure evolution during nanoindentation with initial FRS configuration 3; Stage 2.

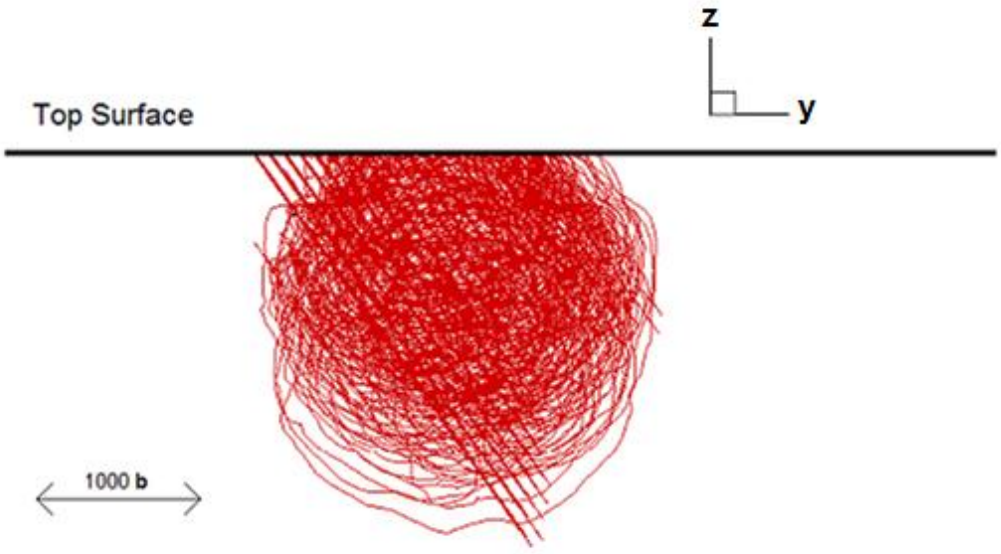

Figure 4.17: Dislocation structure evolution during nanoindentation with initial FRS configuration 3; Stage 3.

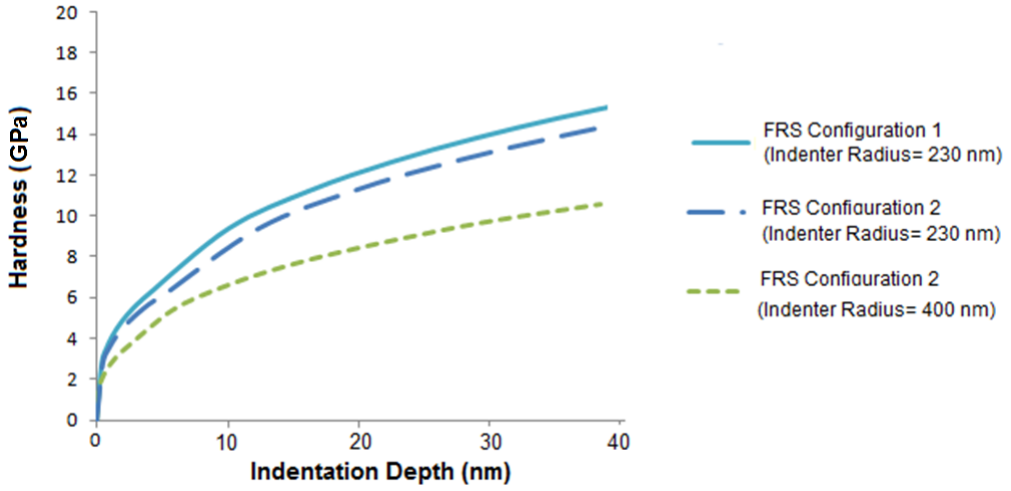

Figure 4.18: Hardness verses Indentation depth for nanoindentation with [001] crystal orientation.

CHAPTER 5

CONCLUSION AND FUTURE WORK

5.1 Conclusion

MDDP can simulate the growth of dislocation structure during nanoindentation. Nanoindentation can be modeled in *MDDP* by utilizing appropriate contact mechanics relations between contact area, contact pressure, loading and indentation depth. Determining the area of contact and proper distribution of load is critical.

The volume distribution of GND depends upon the initial configuration of the dislocation sources. The GND are concentrated into a hemispherical region just surrounding the indentation location for models with an initial dislocation configuration from atomistic simulations. Moreover, there is considerable increase in dislocation density and plastic deformation only in this region. This is because there is high dislocation activity on all slip planes and the cross-slip activity is significant. The patterns on the nanoindented surface formed due to exiting dislocations are symmetric and regular. Moreover, they depend upon the crystal orientation. The height of slip steps decrease progressively away from the indentation axis.

In contrast, for random initial FRS distribution, the volume distribution of GND does not have a well defined shape. The increase in dislocation density and plastic deformation in the nanoindented zone is not significant. The dislocation activity is very low on slip

planes where there is no initial dislocation source present. The topographical maps show the patterns of slip steps to be random and irregular.

Three dimensional dislocation models consider cross-slip and interaction between dislocations on intersecting slip planes. This explains the fact that hardness values obtained using 3D model in this study provide better accuracy than those obtained using 2D models.

5.2 Future Work

Further investigations can be carried out on models where FRS are placed just beneath the surface (near and around the indentation location) since these demonstrate encouraging results. Further simulations can be performed with different indenter types and crystal orientations to evaluate, in depth, the effect of these factors. Secondly, a comparison between a sharp tipped indenter and a round tipped indenter can be studied in detail.

More FRS can be placed just beneath the indenter in a particular sequence as the nanoindentation progresses. This will consider the incidence where homogeneous dislocation nucleation occurs more than once during nanoindentation.

References

1. Oliver, W. C., & Pharr, G. M. (1992).An improved technique for determining hardness and elastic modulus using load and displacement sensing indentation experiments. J. Mater. Res. 7 4, 1992, pp. 1564–1583.

2. Pharr, G. M. (1992). On the generality of the relationship among contact stiffness , contact area , and elastic modulus during indentation, 7(3), 613–617.

3. Ouyang, C., Li, Z., Huang, M., & Fan, H. (2010). International Journal of Solids and Structures Cylindrical nano-indentation on metal film / elastic substrate system with discrete dislocation plasticity analysis : A simple model for nano-indentation size effect. International Journal of Solids and Structures, 47(22-23), 3103–3114. doi:10.1016/j.ijsolstr.2010.07.012

4. Kreuzer, H G M, & Pippan, R. (2007). Discrete dislocation simulation of nanoindentation : Indentation size effect and the influence of slip band orientation, 55, 3229–3235. doi:10.1016/j.actamat.2007.01.021

5. Gane, N. & Bowden, F. P. Microdeformation of solids. J. Appl. Phys. 39, 1432–1435 (1968).

6. Corcoran, S. G., Colton, R. J., Lilleodden, E. T. & Gerberich,W.W. Anomalous plastic deformation at surfaces: Nanoindentation of gold single crystals.Phys. Rev. B 55, R16057–R16060 (1997).

7. Barnoush, A. (2012). Correlation between dislocation density and nanomechanical response during nanoindentation. Acta Materialia, 60(3), 1268–1277. doi:10.1016/j.actamat.2011.11.034

8. Fuente, O.R., Zimmerman, J.A., Gonzalez, M.A., Figuera, J., Hamilton, J.C., Pai, W.W., Rojo, J.M., 2002. Dislocation emission around nanoindentations on a (001) fcc metal surface studied by scanning tunnelling microscopy and atomistic simulations. Phys. Rev. Let., 88, 036101-1.

9. Liang, H. Y., Woo, C. H., Huang, H., Ngan, a. H. W., & Yu, T. X. (2003). Dislocation nucleation in the initial stage during nanoindentation. Philosophical Magazine, 83(31-34), 3609–3622. doi:10.1080/14786430310001605579.

10. Wagner, R. J., Ma, L., Tavazza, F., & Levine, L. E. (2008). Dislocation nucleation during nanoindentation of aluminum, (December), 1–5. doi:10.1063/1.3021305.

11. Joslin, D.L., Oliver, W.C., 1990. A new method for analyzing data from continuous depth-sensing micro-indentation tests. J. Mater. Res. 5, 123–126.

12. Saha, R., Xue, Z., Huang, Y., Nix, W.D., 2001. Indentation of a soft metal film on a hard substrate: strain gradient hardening effects. J. Mech. Phys. Solids 49, 1997–2014.

13. Saha, R., Nix, W.D., 2002. Effects of the substrate on the determination of thin film mechanical properties by nanoindentation. Acta Mater. 50, 23–38.

14. Chen, S.H., Liu, L., Wang, T.C., 2007. Small scale, grain size and substrate effects in nano-indentation experiment of film-substrate systems. Int. J. Solids Struct. 44,4492–4504.

15. Chen, S.H., Liu, L., Wang, T.C., 2005. Investigation of the mechanical properties of thin films by nanoindentation, considering the effects of thickness and different coating-substrate combinations. Surf. Coat. Technol. 191, 25–32.

16. Buckle, H., 1973. In: Westbrook, J.H., Conrad, H. (Eds.), The Science of Hardness Testing and Its Research Applications. American Society for Metals, Metals Park, Ohio, p. 453.

17. Xu, Z.H., Rowcliffe, D., 2004. Finite element analysis of substrate effects on indentation behaviour of thin films. Thin Solid Films 447, 399–405.

18. Cylindrical nano-indentation on metal film/elastic substrate system with discrete dislocation plasticity analysis: A simple model for nano-indentation size effect Chaojun Ouyang Zhenhuan Li , Minsheng Huang , Haidong Fan 2010.

19. Zbib, H.M., Shehadeh, M., Khan, S.M.A., and Karami, G., "Multiscale Dislocation Dynamics Plasticity", Int. J. Multiscale Comp. Eng., 1(1), 73- 89, 2003.

20. Yasin, H., Zbib, H.M., Khaleel, M.A., "Size and boundary effects in discrete dislocation dynamics: coupling with continuum finite element", Mater. Sci. Eng., A309-310, 294-299, 2001.

21. Zbib, H.M., de La Rubia, T.D., "A multiscale model of plasticity", Int. J. Plasticity 18, 1133- 1163, 2002.

22. Khan, S.M.A., Zbib, H.M., and Hughes, D.A., "Modeling Planar Dislocations Boundaries using Multi-scale Dislocation Dynamics Plasticity", Int. J. Plasticity, 20,1059-1092, 2004.

23. Hertz, H., 1896. Miscellaneous Papers by H. Hertz.Macmillan, London

24. The IBIS Handbook of Nanoindentation, Anthony C. Fischer-Cripps, ISBN 0 9585525 4 1, Fischer- Cripps Laboratories Pty Ltd 2009.

25. Boussinesq's problem for a rigid cone, I.N. Sneddon, Proc. Cambridge Philos. Soc. 44, 1948, pp. 492–507.

26. Kreuzer, H. G. M., & Pippan, R. (2004). Discrete dislocation simulation of nanoindentation. Computational Mechanics, 33(4), 292–298. doi:10.1007/s00466-003-0531-3.

27. Kreuzer, H.G. M., & Pippan, R. (2005). Discrete dislocation simulation of nanoindentation: The effect of statistically distributed dislocations. Materials Science and Engineering: A, 400-401, 460–462. doi:10.1016/j.msea.2005.01.065.

28. Kreuzer, H.G.M., & Pippan, R. (2004). Discrete dislocation simulation of nanoindentation: the effect of moving conditions and indenter shape. Materials Science and Engineering: A, 387-389, 254–256. doi:10.1016/j.msea.2004.05.037.

29. Ouyang, C., Li, Z., Huang, M., & Hou, C. (2008). Discrete dislocation analyses of circular nanoindentation and its size dependence in polycrystals. Acta Materialia, 56(12), 2706–2717. doi:10.1016/j.actamat.2008.02.012.

30. Multi-scale Discrete Dislocation Plasticity Analysis: Application to Nano-indentation, Shafique M. A. Khan and Lyle E. Levine, NSTI Nanotechnology Conference and Trade Show 2006, Boston, MA, May 2006.

31. Nibur,K.A.,Akasheh,F.,Nibur,K.A.(2007). Analysis of dislocation mechanisms around indentations through slip step observations, 889–900. doi:10.1007/s10853-006-0007-x.

32. Sun, K., Shen, W., & Ma, L. (2013). The influence of residual stress on incipient plasticity in single-crystal copper thin film under nanoindentation. Computational Materials Science, 1–7. doi:10.1016/ j.commatsci. 2013.08.026

Vitae

Name	: Hassaan Zafar
Nationality	: Pakistani
Date of Birth	: 6/8/1985
Email	: hassaanzafar7@hotmail.com
Address	: Lahore, Pakistan
Academic Background	: B.S Mechanical Engineering (2007) Ghulam Ishaq Khan Institute of Engineering Science and Technology
	M.S. Mechanical Engineering (2014) King Fahd University of Petroleum and Minerals Dhahran, Saudi Arabia